ENGR9700C-D Masters Thesis

Semester 2,2017

Thesis Topic:

The Correlation Between Maximum Shear-strain Analysis and MRI images in Lumbar Disc Herniation

Supervisor:

Associate Professor John Costi

Name:

Sara Panahi

Student Number:

2161330

Word Count (not including coversheet or references):
17,391 words

Abstract

Chronic back pain is a benign, frequent, costly and complex condition which is the second leading cause of Burden of Disease in Australia. Lack of standard therapeutic treatment options for herniated disc and back pain, in general, is a consequence of the limited knowledge in understanding disc failure, although it is commonly believed that certain motions can cause disc herniation in the lumbar region of the vertebral column. A precise perusal of the literature reveals that analyzing the progression of three-dimensional internal maximum shear strains (MSS) in different regions of the disc, during repetitive combined loading can bring insight to understanding the disc failure mechanism. The current multimodal study is designed to investigate disc damage that results from combined motions under repetitive loading using internal tissue displacements and strains supported by magnetic resonance imaging (MRI) assessment.

Eight human lumbar discs underwent pre-test MRI and then were loaded under combined 13 degrees of forward flexion, 2 degrees of right axial rotation and 1.7 MPa compression up to 20,000 cycles or failure at the frequency of 1Hz which is supposed to remodel the heavy lifting in physical work, realistically. Calibration and endplate beads together with circumferential markers were used to identify the periphery of the disc and a wire grid inserted into the mid-transverse plane followed by stereo-radiography technique; then digitizing is performed in neutral position followed by 1, 500, 1,000, 5,000, 10,000, 15,000, 20,000 cycles. A sequence of Matlab codes was used to reconstruct the markers and wires to measure the tissue displacement progression, average MSS and largest principle strain in 9 anatomical regions. Complementary post-test MRI-based grading system is used to score the initiation and progression of the tears and fractures in order to correlate the level of damage to MSS findings in the same nine regions of the disc.

The association between two sets of scores from MRI and MSS analyses obtained in this study could potentially serve for a better understanding of the biomechanical behaviour of the herniated disc and for investigation of the biomechanical aetiology of disc abnormalities (Spearman correlation factor= 0.5966; P<0.001). The high MSS values are located where annular tears fractures and disc bulge are present in MRI image. Additionally, posterolateral region is the common site of failure resulted by combined axial rotation, flexion and compression which validates the findings from computational studies using the same protocol of loading (right posterolateral region experiencing the largest MSS=62%). Finally, comparing the result obtained from alternative methods would be valuable in terms of developing the current surgical methods and procedures, improving the rehabilitation strategies, heavy lifting guidelines and therapeutic implant designs, as well as prevention of the segmental instability and back pain.

Acknowledgement

Declaration

'I certify that this thesis does not incorporate without acknowledgment any material previously submitted for a degree or diploma in any university; and that to the best of my knowledge and belief it does not contain any material previously published or written by another person except where due reference is made in the text.'

Panahi

October 16th, 2017

TABLE OF CONTENTS

List of Tables

List of Figures

Chapter 1: Previous studies

This chapter gives the brief introduction of the disc structure followed by the literature of disc herniation mechanism and the existing knowledge of potential loading scenarios and common sites of the failure; which provided useful information to design the framework of the current study.

1.1. Lumbar Region and Disc Structure

The spinal column is a substantial structure that provides support and mobility to the upper body; it also enables sliding, bending and twisting in 6 degrees of freedom. The vertebral column is made of 29 vertebras, intervertebral disc (IVDs) muscles and ligaments. Although sharing a common shape, each set of vertebras is categorized into cervical, thoracic, lumbar, sacrum and coccyx regions according to its particular structure and function (Figure 1.1). This study focuses on the Lumbar region of the vertebral column located between the thoracic and the sacrum which consists of five vertebral bodies (L1-L5) and intervertebral discs (IVDs) between adjacent vertebral bodies. As shown in Figure 1.1.b, the vertebras in lumbar region are mainly kidney shape with a larger cross-sectional area since they are required to withstand

(a)   *(b)*
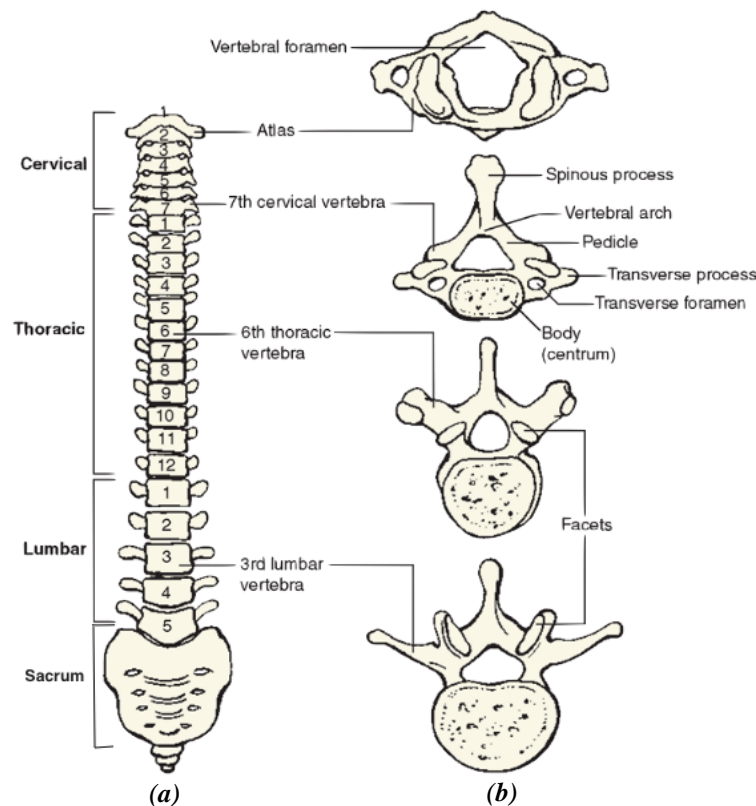
Figure 1.1. (a) The front view of the vertebral column **(b)** Different shape of vertebrae from different regions from top view (*Vertebrae shape across various regions,* n.d.).

1

the highest amount of compressive loads from the biomechanical point of view. A study by Singel et al. (2004) demonstrates that by moving from L1 to L5 the width of lumbar pedicles increase while their height is decreased. According to the recent study, L5 pedicle represents the largest cross-sectional area and the shortest height to resist the body weight and other vertical loads. Intervertebral disc is made of nucleus pulposus (NP) at the centre, surrounded by concentric lamellar layers known as annulus fibrosus (AF) and the hyaline cartilaginous end plate toward the vertebral body (Figure 1.2). The disc has a strong and flexible structure which is responsible for adjoining the vertebral bodies and transferring the vertical loads throughout the vertebral column while it enables twisting and bending. The gel-like nucleus is mostly made by water (70-90%), proteoglycans (PGs) (14%) and collagen (mainly type II) (4%); while, annulus is made of water (60-70%), highly oriented collagen type I (50%) and PGs (5%) (Bogduk 2005). It is believed that the semi-fluid nucleus structure would transfer the compressive load through the annulus walls circumferentially and to the endplates from there (Humzah & Soames 1988; Bogduk 2005). However, the disc is constantly loaded under six-degrees-of-freedom (6DoF) forces and moments which makes the analysis more complex. IVDs in lumbar region are known to be the common source of chronic back pain (Kuslich et al. 1991).
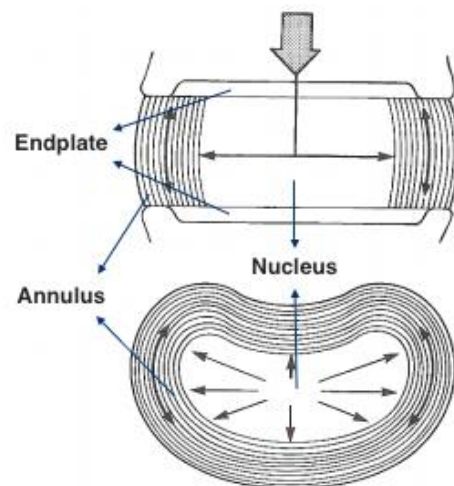
Figure 1.2. Sagittal (top) and axial (bottom) view of the IVDs under pure compressive load. Blue arrows are showing the position of the nucleus, annulus and the endplate in the disc; the black arrows are showing the compressive load transmission from nucleus to annulus and endplate.

1.2. Low Back Pain (LBP)

According to the Australian Institute of Health and Welfare (AIHW) statistics, chronic LBP is reported as the second common chronic disease in 2011 to 2012 after arthritis. The same study reports that the number of 2,805,500 people (12.7% of the Australian population) has suffered from back pain in 2011-2012; moreover, it is estimated that about 70 to 90% of people would suffer from LBP at least once in their lifespan. A recent national survey in years 2014 and 2015 shows that 1 in 6 Australians (16% of

the total population) reported some kind of back problems at some point in their lives which comes to 3.7 million people; while it still has a big gap with osteoarthritis with the rate of 9.0% (2 million of the entire population), 3.5% osteoporosis and 1.8% rheumatoid arthritis (AIHW 2016). Although back pain is not a fatal disease, it is believed that it is strongly related to the quality of life by affecting the level of activity and physiological distress. Findings from Quittan study (2002) demonstrate that 14% of people with chronic back pain experience the constant pain while the rest (86%) would suffer the pain at least once a week. Back pain has reported as the second greatest non-fatal leading cause of burden of disease (BoD) in men after musculoskeletal conditions with 420,734 Disability-adjusted life years (DALYs) in 2011 (AIHW 2016). In addition, as reported by the AIHW, people with back complexities are 3.2 times more likely than the general population to experience poor health and also 1.8 times more likely to have a very high psychological distress in their lives (AIHW 2016).

There are many variables need to be considered in studying the chronic back pain. It is a multifactorial issue that can caused by genetic, pathological, sociological and environmental factors as well as mechanical and biomechanical factors. Age, the level of fitness, lifestyle, smoking history and also genetic elements are known as back pain risk factors (Raspe et al. 2004; Williams et al. 2013). In general, chronic diseases, back pain included, can never be completely cured. This is why a comprehensible long-term treatment plan in primary health care is critical to manage the pain and to prevent further injuries. Back problems can be caused by wide range of injuries or conditions such as posture associated issues, diseases such as osteoarthritis, osteoporosis, disc disorders (such as
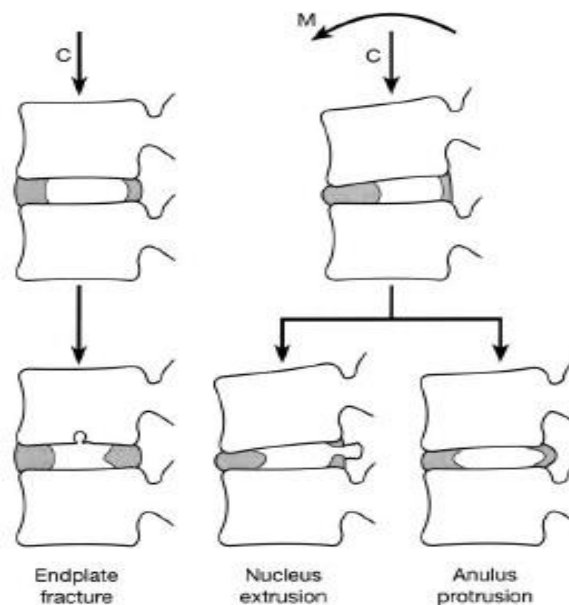
Figure1.3. Schematic major modes of disc herniation (Costi, et al. 2007): endplate fracture, nucleus extrusion and annulus protrusion (or disc bulge). Combined compression and forward bending can cause either nucleus extrusion or annulus protrusion while the pure compression may lead to the endplate fracture. (Costi, et al. 2007).

degenerated or herniated disc), muscle strain or even some genetic conditions. One common disc complexity is the disc herniation which is involved in 20-75% of the patients with the LBP, depending on the author's definition (Jensen et al. 1994; Beattie & Meyers 1998). Herniation in this study is defined as an extrusion of the nucleus, which can cause deformation and change in the profile of the disc as shown in Figure 1.3. According to AIHW (2010), herniation is somehow involved in one-fourth of all the work-related injury claims as a result of certain repetitive motions which cost about three billion dollars in 2008 and 2009 (ABS, 2013a).

Beattie & Meyers (1998) argues the disc bulge, protrusion and extrusion (previously discussed as herniation) are the most common disc abnormalities which can be diagnosed using the MRI images as reported in Table 1.1. Jensen et al. (1994) showed that disc bulge or protrusion cannot necessarily cause the LBP, as many people are suffering from these two, do not experience the chronic back pain. On the other hand, extrusion might lead to nerve compression which is associated with chronic LBP (Beattie & Meyers 1998). Despite the fact that the disc is the largest aneural and avascular structure in the body, few studies have addressed the annulus tears and disruptors as the initial source of failure which leads to the LBP due to its outer vascular portion (Osti & Fraser 1992; Ricketson et al.1996; Schellhas et al. 1996). Although there are many studies conducted to clarify the mechanism of the disc herniation, it still remains unclear due to the bi-phasic, time-dependent nature of the disc structure and also its various responses to different motions and loading conditions.

Table 1.1. *Terminology of main disc abnormality evaluated by MRI imaging technique (Beattie & Meyers1998).*

Classification	Criterion
Normal	No disk extension beyond the interspace
Bulge	Circumferential, symmetric extension of the disk beyond the interspace (around the vertebral end plates)
Protrusion	Local or asymmetric extension of the disk beyond the interspace, with the base against the disk of origin broader than any other dimension of the protrusion
Extrusion	More extreme extension of the disk beyond the interspace, with the base against the disk of origin narrower than the diameter of the extruding material itself or with no connection between the material and the disk of origin

Conclusively, back pain which has a relatively high risk of likelihood has been placed second on the Burden of Disease list in Australia after cancer and cardiovascular disease, nonetheless seems not to be treated scientifically. The lack of knowledge in understanding the mechanism of back pain and disc

failure has caused the use of a wide range of therapeutic procedures which are not necessarily successful (Quittan 2002). The protocol of loading as well as certain motions that can cause the disc to prolapse, the mechanism of failure and the possible initial failure regions, are to date, unclear. However, certain motions and protocols of loading are suggested by different studies which place the disc at greatest risk of failure and herniation (Adams et al. 1994; Callaghan & McGill 2001; Costi, et al. 2007; Berger-Roscher et al. 2017). The following review mainly addresses certain motions, loading protocols, the degenerative condition required to fail the disc and also methods used in various studies in order to evaluate the level of damage.

1.3. Motions - Protocol of loading

A seminal in-vitro study by Adams et al. (1994) demonstrated that the lack of support from posterior elements might place the disc at risk of failure under bending fatigue loading. It noted that the consequent disc failure occurs at the outer posterior region of the IVD. Few other studies argue that the pure compression itself cannot herniate the disc; however, the combination of compression coupled with bending (simulating the forward bending and lifting which is presented in heavy physical work) can cause the disc to fail in cadaver and animal-based experiments (Kelsey et al. 1984; Kumar 1990). In fact, pure compression has been reported by several studies to damage the vertebra or endplate prior to damaging the IVD (Brinckmann 1986; Hansson et al. 1987; Liu et al.1983). Adams et al. also suggest that the flexion repetitive loading would cause damage to the outer posterior annulus at the mid-disc height. Finally, Adams et al. conclude that under fatigue bending load, the nucleus internal pressure increases, which causes the nucleus to migrate towards the peripheries of the posterior regions.

Callaghan & McGill (2001) conducted an in-vitro experiment to examine if the low-magnitude forces and moments can lead to herniation of the healthy, non-degenerated IVDs in the cervical region. The experiment designed to load the disc under 260 N of compression and 86,400 flexion cycles followed by x-ray images at intervals to track the herniation and finally dissecting the disc horizontally to observe the tissue damage by injecting the blue dye prior to cutting the frozen disc open. Callaghan & McGill observed the nucleus protrusion in posterior and posterior-lateral regions of the annulus under repetitive flexion/extension applied with axial compression. In addition, findings from sequential x-rays reveal that the interior end plate- annulus junction is the first region that fails which propagates to the exterior border during the fatigue loading. Furthermore, they outlined all the factors required for disc herniation such as motions, orientation and number of cycles in fatigue loading besides the level of degeneration of the IVD. Finally, Callaghan & McGill conclude that a modest amount of compressive force only

when it is coupled with adequate flexion/extension can cause a cumulative process that can lead the herniation. Findings from Callaghan & McGill also highlighted the critical role of flexion and extension in herniating the degenerated disc in addition to the axial compression, which acknowledges the findings from previous studies. Although Callaghan & McGill compressive study provides insight into the mechanism of disc failure from many aspects, the experiment is limited to flexion/extension in the sagittal plane, however, the spine movement is within 6DoF.

A study by Wilder et al. (1988) demonstrated the herniation under a combination of flexion, axial rotation and lateral bending in static or vibration protocol of loading. The most significant finding from this study addressed the tracking tears to originate in the nucleus where they gradually propagate through the posterior-lateral region of the annulus. A recent study confirms the finding from the previous study by observing the microstructure of 29 ovine lumbar IVDs subjected to high-frequency vibration loading ($1300 \mp 500\ N$ at 5Hz between 20,000-120,000 cycles) (Wade et al. 2016). However according to Wade et al., the damage initiated at inner and mid annular layers in both anterior and posterior regions which then leads to the nucleus protrusion.

A recent study by Berger-Roscher et al. (2017) has been conducted to investigate which type of loading can lead to different modes of failure in the ovine specimen. It can be concluded based on this study that the cyclic, complex loading (combination of flexion, lateral bending, axial rotation and axial compression) could potentially cause endplate failure caudally, however, the combination of compression used with axial rotation or lateral bending most likely lead to posterior outer region of the annulus to fail. Additionally, it is suggested that the most common site of failure is endplate junction followed by the failure of annulus. Berger-Roscher et al. (2017) also announced the key point in herniation is the combination of flexion and lateral bending. According to their findings, a complex loading condition missing either of these two is considered completely safe as it has been reported with the lowest risk of failure. Another in vivo study by Rajasekaran et.al (2014) confirms the recent conclusion by the Berger-Roscher et.al (2017) study about the failure regions. According to the recent study in 65% of herniation cases, the endplate junction is involved (type I), however, in the rest of failures (35%) annulus rupture or avulsion of endplate is responsible for the disc herniation (type II).

Referring to the above discussion, it seems that the majority of studies found the combined protocol of loading (the combination of compression with lateral bending, axial rotation and flexion) which can lead to disc herniation (Adams 1982; Costi et al. 2007; Wilke et al. 2016). On the other hand, among all the protocols tested in various studies such as vibration (Wilder et al.1988; Wade et al. 2016),

repetitive (Callaghan & McGill 2001; Kelsey et al. 1984; Adams et al. 1994; Costi, et al. 2007; Berger-Roscher et al. 2017) and sudden loading (Wade et al. 2015), cyclic repetitive combination of forces and moments seems to be the most appropriate loading protocol in modeling manual handling in labor work.

1.4. Maximum Shear Strain (MSS) Analysis

Shear strain analysis is a common approach in investigating the disc deformation under certain loading conditions until the failure occurs. It is believed that the maximum shear strain (MSS) is most likely the major perceptible evidence of the disc failure (Costi et al. 2007). Seroussi et al. (1989) calculated the two-dimensional internal displacement of the disc in the mid-sagittal plane. Tsantrizos et al. (2005) also investigated the influence of nucleus migration on intra-discal strains in the mid-transversal plane during compressive and bending conditions. Both of the above-mentioned studies were limited to two-dimensional strain analysis in sagittal and transverse planes.

Costi et al. (2007) provided a useful insight into the biomechanics of the disc by establishing a method to measure the three-dimensional internal MSS and reports the regions with the greatest strains which place the disc at the highest risk of failure. Similarly, Tsantrizos et al. (2005) note that the variation of the MSS values in different regions of the disc can be an evidence of tissue deformation (such as nucleus pulpous migration). This would be helpful in understanding the mechanism of the disc failure which can cause segmental instability and low back pain. This goal can be achieved using the Stereo Radiography (SR) technique to track and quantify the deformation in different anatomical regions of the disc after a certain number of cycles. Both inside and periphery of the disc tissue are tagged using a tantalum wire grid and landmarks (calibration, endplates and circumferential markers), respectively. Up to either a certain number of cycles or just after observing a significant change in the displacement in Z-axis under loading (which is an evidence of disc failure), the specimen is unloaded and the average of MSS of the tissue is calculated.

In MSS analysis the displacement of the landmarks is calculated based on the neutral position and been normalized by displacement (mm) or rotation (°) under combined loading scenarios. According to Costi et al. (2007) lateral bending and compression cause the largest regional MSS. It is reported that the posterior, posterolateral and lateral regions of the IVD represent the highest amount of MSS (See Figure 1.4); while the results are slightly different for biological MSS; as bending and flexion produce the largest MSS that can place the disc into the risk of failure (Costi et al. 2007). The last finding from this study perfectly lines up with the previous study by Adams et al. (1994) and the recent study by Berger-

Roscher et al. (2017). Likewise, Tsantrizos et al. (2005) demonstrate the linear relationship between the segmental angle of lateral bending and the increase in nucleus migration. Furthermore, the same study argues that lateral bending loading condition would cause the nuclear migration that may lead to the segmental instability in the disc.
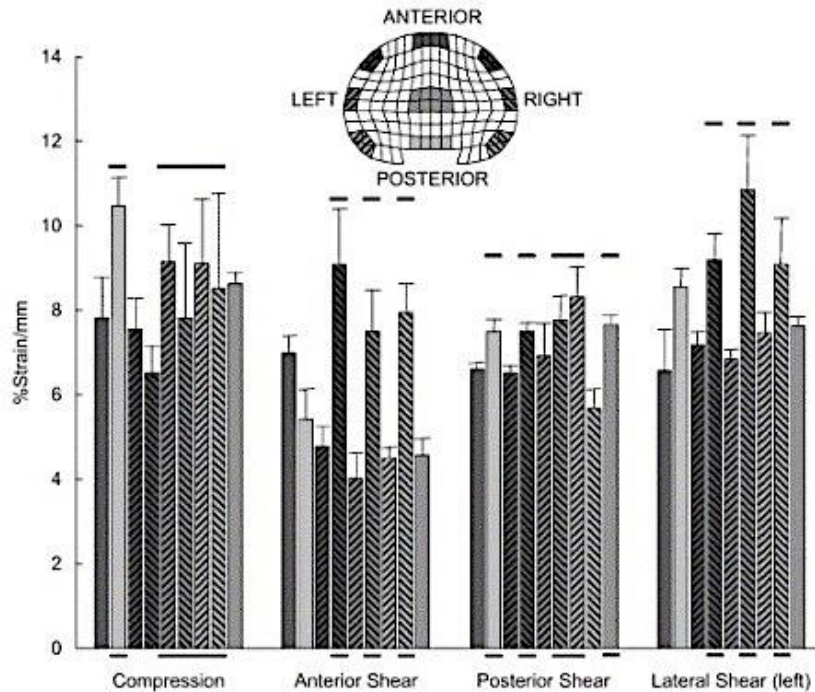
Figure 1.4. The effect of isolated pure forces and moments on the anatomical disc regions. Lateral shear and compression in the lateral and posterolateral regions produced the largest MSS per mm of displacement (Costi et al. 2007).

A recent in-vivo study by Yu et al. (2016) conducted to investigate the range of disc deformation in the cervical region under flexion and extension in ten subjects using both MRI images and measuring the MSS in and around the disc. Similar to the SR technique, a dynamic image of the cervical vertebras was obtained using two fluoroscopes positioned orthogonal to each other in the latter study. Yu et al. (2016) also suggest that the variation of the distribution of the MSS need to be monitored in five anatomical regions of the cervical disc as anterior, centre, posterior, left and right during the loading. These five regions are adequate for discussing the results in cervical discs, however, nine (anterior, posterior, nucleus, right lateral, left lateral, right anterolateral, left anterolateral, right posterolateral and left posterolateral) anatomical regions are suggested by the majority of studies in lumbar spine due to its larger cross-sectional area.

1.5. MRI Analysis

Among all the imaging systems, magnetic resonance imaging (MRI) has become the most common tool used in the diagnosis of disc abnormalities in the lumbar spine. Even though the tissue with the reasonable amount of fluid responds to the magnetic field perfectly, gas or solid contents such as air and cortical bone do not allow the alignment of T1 and T2 weighted scans. MRI is considered as a safe (non-ionizing), non-invasive technique with the minimum risk for the patient in comparison with other imaging systems. It provides high contrast and high-resolution images with the reasonable signal-to-noise ratio and low motion artifact in multi-axial, multiplanar which enable the study of anatomy and biochemistry of the disc (Beattie & Meyers 1998). Beattie & Meyers argues that the shape or the water content of the tissue in MRI image may indicate an abnormality in the disc. Since nucleolus and annulus are different in the amount of hydrogen atom content, both T1 and T2 are commonly used to optimize the contrast between different regions of IVD (Beattie & Meyers 1998). Signal intensity varies based on the chemistry of the subjected tissue and the water content; Table 1.2 interprets the bright to the dark grey level of MRI image voxels, particularly in Lumbar region (Beattie & Meyers 1998). E.g. in T2 weighted images nucleus can be recognized by its relatively high intensity at the centre while the annulus can be distinguished by low-intensity or dark grey signal.

Table 1.2. Signal intensity interpretation in T1 and T2 weighted image (Beattie & Meyers 1998).

Structure	T_1	Proton Density	T_2
Fat	High	High	Low
Marrow	High	High	Low
Cerebrospinal fluid	Low	Intermediate	High
Nerve	Intermediate	Intermediate	Intermediate
Muscle	Intermediate	Intermediate	Intermediate
Hyaline cartilage	Intermediate	Intermediate	Bright
Fibrocartilage	Low	Low	Low
Ligaments	Low	Low	Low
Nucleus pulposus	Intermediate	Intermediate	High

MRI analysis enables the diagnosis of the bulging disc, focal protrusion, nucleolus extrusion and annular tears in the disc. An unpublished study by Amin et al. (2016) developed the observation-based technique to diagnose the disc bulge in the cadaver specimens based on pre- and post-failure MRI images under specific loading condition in both sagittal and axial views (see Figure 1.5). Another study by Mayerhoefer et al.

(2012) was conducted to distinguish between disc abnormalities (normal, bulging and herniated lumbar discs) from each other, using morphological T1weighted images besides texture and geometry analyses using T2 weighted maps.
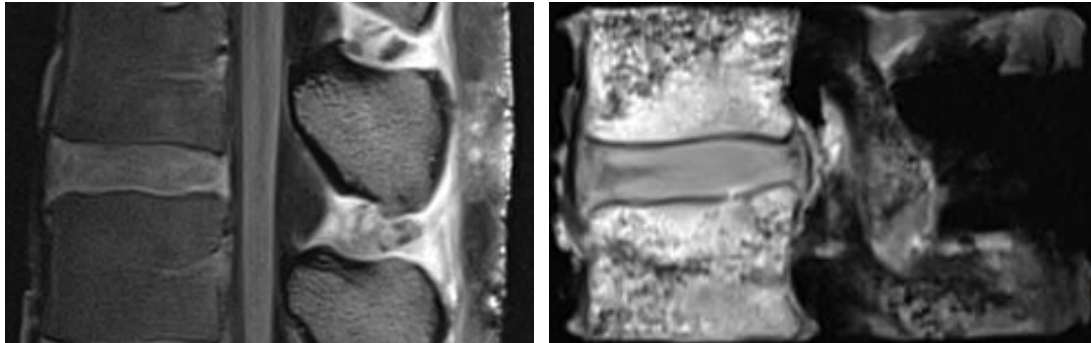
(a) Pre-MRI   *(b) Post-MRI*

Figure 1.5. *Pre- and post- T1 weighted MRI images from sagittal view in left and right, respectively (Amin et al. 2016). Posterior bulge can be seen in post-MRI image while pre-MRI image indicating the normal healthy disc.*

In conclusion, Beattie & Meyers (1998) states that even though the use of MRI methodology in LBP is still controversial, it has an undeniable success in diagnosing the degenerated and herniated disc. In the end, Beattie & Meyers conclude that even though MRI provides very useful morphological information of the disc, findings from MRI analysis need to be linked and compare with other clinical examinations in order to make a reasonable conclusion. In other words, MRI and other complementary tools are required to conjugate with other techniques to provide more informative findings.

1.6. Macroscopic Analysis

The level of damage can be inspected visually in each transaxial slices of the disc after failure by cutting the disc open. Visible evidence of rupture and fracture are classified in terms of their severity. An early study in 1997 (Vernon-Roberts et al. 1997) investigated the level of disc damage by slicing the disc into four layers with the relatively same thickness in nineteen human cadavers. Vernon-Roberts et al. developed a grading system to classify the pathogenesis of tears in the disc using multiple-level transracial analysis of the T12-L1 disc. Amin et al. (2016) also used the similar set of slices to score the level of tissue damage, visually. Figure 1.6 illustrates the three slices made by two axial cuts with identical distance from the vertebral body which were used for the observation-based macroscopic analysis from the latter study.

Figure 1.6. *Transaxial slices with different level of damage throughout the annulus (Amin et al. 2016)*

Reviewing the literature suggests that the nucleus protrusion via endplate junction and inter-laminar tear are the most common modes of disc damage under the repetitive protocol of loading, which mainly occurs in lateral and posterior regions of the disc (Costi et al. 2007; Wade et al. 2014). Table 1.3 represents a brief summary of the most significant background studies in this field. It can be inferred from the table that the majority of the studies agree that the initial site of the rupture is annulus fibrosus (Adams et al. 1994; Challaghan & McGill 2001; Costi et al. 2007; Wade et al. 2014- 2015); however, Wilder et al. (1988) and Transzios et al. (2005) reported the nucleus displacement prior to any other changes in the IVD. Moreover, Adams et al. (1994), Berger-Roscher et al. (2016) and Wade et al. (2014) observed the failure exclusively in the posterior region; nevertheless, the rest of studies found the failure at posterolateral region of the disc (Wilder et al. 1988; Challaghan & McGill 2001; Costi et al. 2007; Wade et al. 2014- 2015) and only Transzios et al. announced the failure at lateral region resulted by the combined compression, extension, flexion and left lateral bending loading condition. Apart from experimental studies, an FEA (finite element analysis) study by Schmidt et al. (2007) confirmed the posterolateral regions undergoing the highest intra-discal pressure and strain under combined loading.

Table 1.3. Literature review comparison table of the most significant studies; different methods were used to investigate the level of disc damage under various motions and loading conditions applied to cadaver or ovine spine segments, resulting in different initial failure sites and structure.

Index	Author	Year	Specimen	Motions	Loading protocol	Initial site of rupture	Damage origin	Method
1	Wilder et al.	1988	Human cadavers	Combined lateral bending, flexion and axial rotation	Vibration loading	Nucleus through the posterolateral region of the annulus	Posterolateral region	Biomechanical properties measurement
2	Adams et al.	1994	18 cadaver motion segments (L2-L5)	Combined compression (1,129 ± 255 N) and Forward bending (flexion angle of 14.8° ±	Linear ramp loading/unloading cycle (2 seconds, under displacement control)	Annulus	Outer posterior in the vertical direction at mid-disc height	2D actuator
3	Callaghan & McGill	2001	26 non-degenerated porcine cervical spines (C3- C4)	Flexion/extension moments, angular rotations and compressive forces	Repetitive Max 86 400 bending cycles at a rate of 1 Hz	Annulus	Posterior and posterior- lateral	2D testing apparatus, interval x-rays
4	Tsantrizos et al.	2005	5 human L1/S1 lumbar spines	10 Nm lateral bending, 500 N axial compression	5 loading and unloading steps: Compression, extension, flexion, left lateral bending	Nucleus pulpous migration	Lateral, to the opposite side of the bending (Right)	1.MSS at mid-transversal plane 2. MSS Analysis, Stereo radiography
5	Costi et al.	2007	9 human lumbar discs	Axial compression, ±5.3° flexion, ±2.5° axial rotation, ±4.8° lateral bending	Sequence of 10 min ramp	Annulus inter- lamellar	Posterior, posterolateral and lateral peripheral	
6	Wade et al.	2014	72 healthy mature ovine lumbar spines	10° flexion and an elevated rate of compression	Displacement rate of 2 mm/min (low) or 40 mm/min (high)	Mid-then-outer Annulus	Posterior	Microstructural analysis
7	Wade et al.	2015	24 mature ovine lumbar segments	10° of Flexion	Sudden (5mm displacement in 0.75 seconds)	• Annular endplate junction (58%) • Annular rupture (25%) • Endplate fracture (17%)	Posterolateral	Microstructural Analysis, Video and sound
8	Berger-Roscher	2016	Thirty ovine lumbar spinal segments	08–138 flexion, 08–108 lateral bending, 08–48 axial rotation, 0–800 N axial compression	1000 cycles at 2 Hz	•EPJ failure (76%) •Annulus failures (24%)	Caudal EPJF	Ultra-high field MRI, Micro-CT scanner

1.7. Objectives

It appears there is no comprehensive study that analyses the disc failure using a combination of methods. Subsequently, this prospective study was designed to investigate the correlation between engineering (MSS analysis), clinical (MRI images) and histology (macroscopic analysis) points of view under combined fatigue loading condition; however, the macroscopic approach could not be achieved due to the time limitation of the masters candidature . Therefore, the first aim of the current study is to investigate the meaningful relationship between MSS and clinical analyses of MRI images under combined forward flexion, right axial rotation and compression in cadaver specimens. The second aim of this study is to address the initiation failure site and progression of the disc damage as well as the failure mode under this loading scenario.

It is expected that the highest magnitude of maximum shear strain within the nine anatomical regions is associated with the signal intensity changes in MRI image where circumferential and radial tears and bulges are present. The Spearman correlation factor and two-tailed P value have been calculated in order to determine the strength of the relationship between MSS and MRI scores statistically. The logical explanation behind it, is that the significantly higher maximum shear strain within disc regions can potentially develop the tears (seen from MRI images) which can be evidence of the disc failure.

Chapter 2: Methods

2.1. Dataset

This study is part of a comprehensive study with the total number of thirty-two cadaveric lumbar FSUs (functional spinal unit) with facet joints that has divided into two groups of sixteen. So that, each group undergo a different loading scenario tending to examine the mechanism of disc failure under combined flexion and compression coupled with either lateral bending or axial rotation. Additionally, the comprehensive study was also designed to investigate the effect of wire grid on the mechanical properties; therefore, the specimens are divided into two wired and control groups. The control group consists of eight specimens (six males and two females) for each direction of loading. Hence, the total number of sixteen-wired and sixteen-control specimens were planned to be loaded. The total number of eight specimens were used for the current study from the wired group which underwent the combined flexion, axial rotation and compression. The grade of disc degeneration for all the specimens is reported to be two based on Pfirrmann classification of IDD (inter-vertebral disc degeneration), which is interpreted as mildly degenerated discs (Pfirrmann et al. 2001) (see Appendix A).

The sequential series of tasks were performed in the main study for the entire dataset such as pre-MRI image, preloading the disc, wire grid insertion, performing the hexapod experiment, stereo-radiography (SR), wire digitizing, three-dimensional disc reconstruction followed by the post-MRI image. The FSUs were potted and fixed in PMMA and then kept in the saline bath at 37°C with the compressive pre-load of approximately 0.1 MPa applied on the disc overnight for about 20 hours (Amin et al. 2015). The exact preload compressive force has to be calculated exclusively for each specimen considering the cross-sectional area of the disc. Afterwards, the vertical disc displacement is calculated after preload is been applied and has to be reported by the examiner for further calculations. Later, the endplates and periphery of the disc are tagged by markers the tantalum wire grid is inserted along the mid-transverse plane to be recognized by
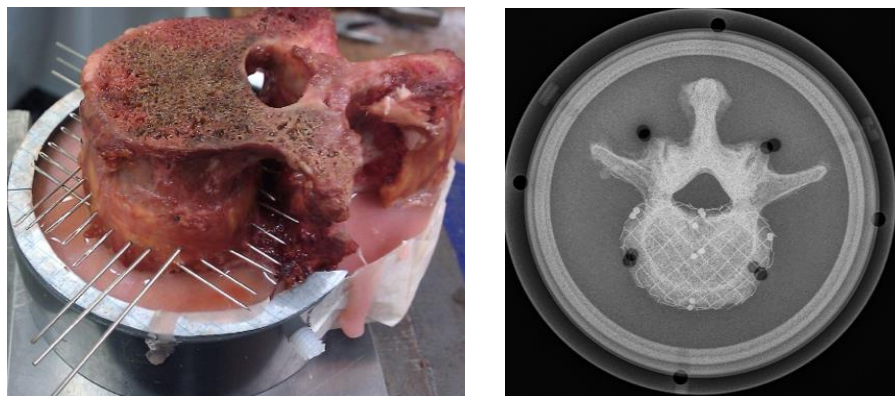
Figure 2.1. *The tantalum wire grid insertion using long needles at 5mm intervals of the mid-transverse plane at 45 degree (left) (Costi et al. 2007) The X-ray radiograph is showing the wire grid and endplate visible radiographic beads from axial view (right) (Amin et al. 2015).*

14

digitizing process in order to proceed the MSS analysis (see Figure 2.1). The tantalum wire grid with approximate 5 mm intervals usually consist of 6×6 wires were inserted in the mid-transverse plane at the degree of 45. In general, the bigger the disc, the more wires are required to digitize the tissue. All the experimental data corresponds to eight cadaver specimens are kindly provided by Dhara Amin for the current study (see Table 2.1).

Table 2.1. Dataset: Eight cadaver specimens were loaded up to 20,000 cycles or failure; the number of 10-13 wires and 13-20 circumferential markers were used for each specimen.

Specimen Number	Specimen ID	Disc level	Final cycle	Tantalum Wire grid	Circumferential markers
W12	5029	L3-4	10,000	6×6	13
W13	5003	L2-3	500	6×6	15
W15	5029	L1-2	5000	6×6	16
W16	4571	L4-5	10,000	6×5	14
W18	4550	L2-3	10,000	7×6	16
W21	3582	L3-4	1000	6×7	17
W23	4571	L2-3	20,000	5×5	15
W25	4696	L2-3	500	6×6	20

According to Dhara Amin, all the specimens were loaded up to 20,000 cycles or until failure although the majority of the specimen failed before reaching that stage. The vertical displacement of the hexapod along the z-axis is an indicator of the disc or vertebral body failure. Hence, the displacement of over 4 mm along the z-axis is defined as the disc failure and the user stops the experiment just after observing such a significant vertical displacement. The number of wires and landmarks depend on the disc dimensions; however, some complexities in the digitizing process are inevitable which can also affect the number of landmarks. E.g. specimen number W23 used to have a 6×6 wire grid, originally. Two of the wires (wire number 4 and 12) in the grid worn out during the experiment after cycle 5000. However, omitting the two worn wires in all the cycles would potentially cause large errors in further measurements, the number of wires and markers must be identical throughout the digitizing process for each specimen. Therefore, the grid size has updated to 5×5 for all the sequences.

2.2. Hexapod- Combined loading protocol

A custom made hexapod machine is used to load the FSUs under combined 6DoF forces and moments (Costi et al. 2007; Stokes et al. 2002). The direction of loading for all eight specimens in this study was 13 degrees of flexion, 2 degrees of axial rotation and 1.7 MPa compression at the frequency of 1Hz which

was realistic flexion and rotation plus compression equivalent to the internal disc pressure while lifting a 20 kg box (Pearcy et al. 1984). This experiment was designed to remodel the heavy lifting in physical activities in order to investigate the work-related disc injuries in real life. The experiment was performed by Dhara Amin and were stopped at certain intervals (cycle, 1, 500, 1,000, 5,000, 10,000, 15,000, 20,000) and x-ray images were taken using the stereo radiography technique.

2.3. Stereo Radiography (SR)

A pair of x-ray tubes with corresponding flat panel digital detectors were positioned around the disc. Figure 1.4 demonstrates the schematic and real adjustment of two x-ray tubes around the specimen in SR technique. The specimen is subjected to the x-ray beam at its neutral position followed by 1, 500, 1,000, 5,000, 10,000, 15,000 and 20,000 or until failure.
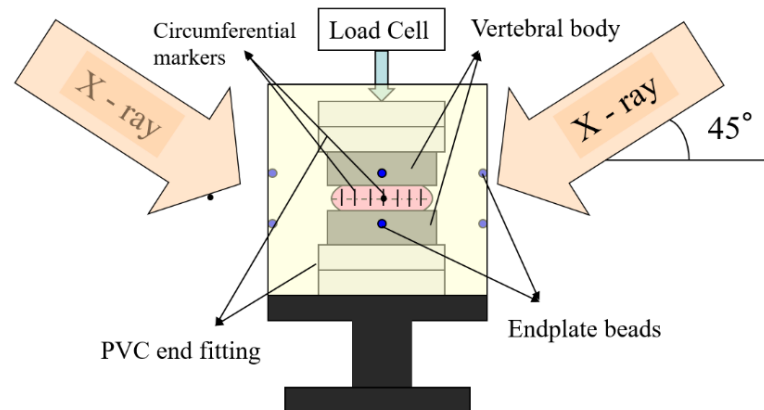
(a)
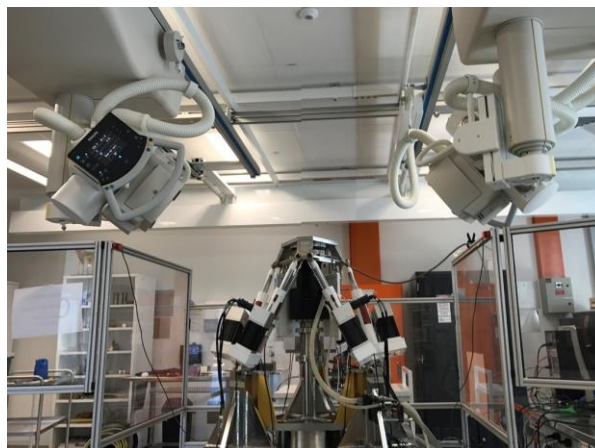
(b)

Figure 2.2. *Stereo Radiography (SR) technique. **(a)** Schematic and **(b)** real set up of x-ray tubes in the biomechanics laboratory at Flinders university (Costi et al. 2007). The x-ray tubes are placed at 45 degrees with respect to the horizon around the specimen.*

The resultant x-ray left and right images were taken by Dhara Amin; labelled and saved as .jpeg format, separately for digitizing purposes performed by the author. Figure 2.3 illustrates the left and right x-ray images of one of the specimens used for three-dimensional reconstructing of the disc wire grid and its periphery.

a) Left   *b) Right*
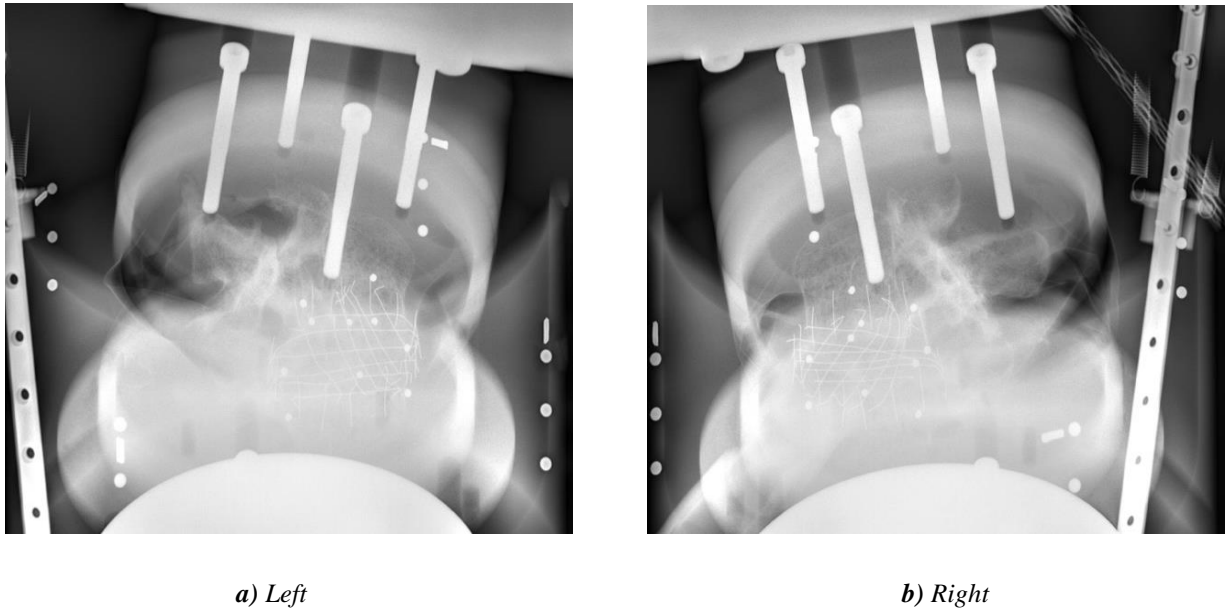
Figure 2. 3. *Left and right pair of x-ray images provided by stereo radiography technique for specimen number W23 after 1,000 cycles.*

2.4. Wire Digitizing

Wire Digitizing software is originally written in Matlab programming language (The Mathworks Inc., Natick, MA, USA) that uses the stereo left and right pair of x-ray radiographs in jpeg format to identify the calibration points, endplate beads, circumferential markers and the wire grid manually. All the digitizing work is performed by the athor in this study. The total numbers of twelve calibration points on the top and bottom holder plates are recognized by the software for both left and right images, in the first step. As shown in Figure 2.5, the order of the calibration beads is dissimilar in left and right images.

| a) Left | b) Right |
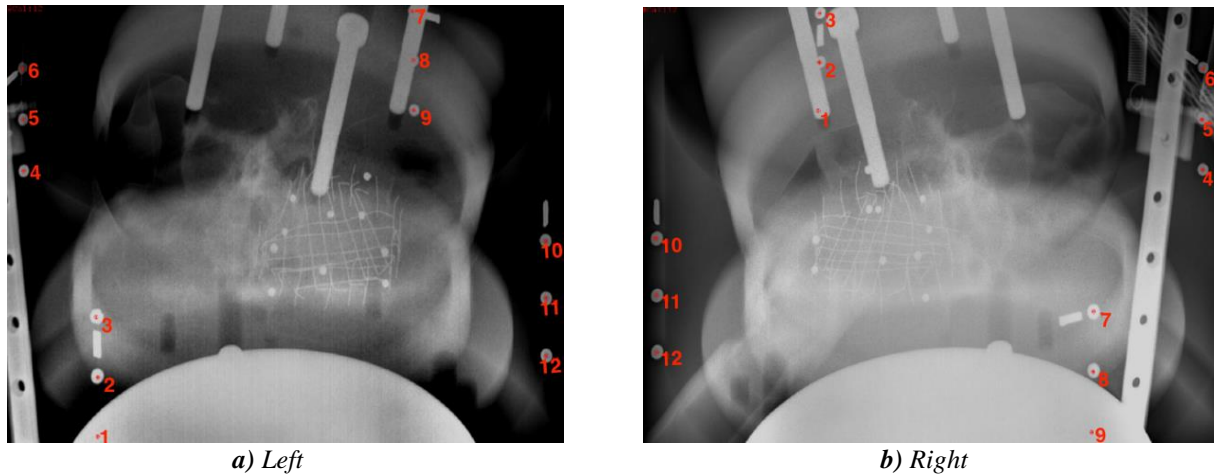
Figure 2.4. *The order of 12 calibration beads with 2 mm diameter for both Left and Right x-ray radiographs for specimen W15 (cycle 1000).*

Next step is identifying the ten end plate beads in order to find the position and also deformation of the disc endplate. The software automatically detects the beads with the highest contrast within the adjustable square field which is not always correct. Therefore, the user needs to double check the calibration beads and endplates after recognized by the software. The most time-consuming step is detecting the wires for both images which has to be done manually. The number of nine points is originally defined by the software as a default. The maximum number of forty beads per wire was chosen for all the specimen in this study. There is no general rule for placing the points on the wires; however, curve wires compare to more predictable flat ones require more points for digitizing. Similar to the calibration beads, the order of wires alters from right to left images.

Finally, a ring of 14-20 circumferential markers is placed around the entire wire grid so as to determine the periphery of the disc. The total number of circumferential markers has to be identical for the same specimen under different cycles of loading. It is quite likely that circumferential markers are lost or misplaced during the experiment; therefore, it is recommended to start the digitizing from the final cycle (20,000 if available). In addition, the number of wire intersections, circumferential markers and also the length of the wires in right and left images, has to remain consistent over cycles.

18
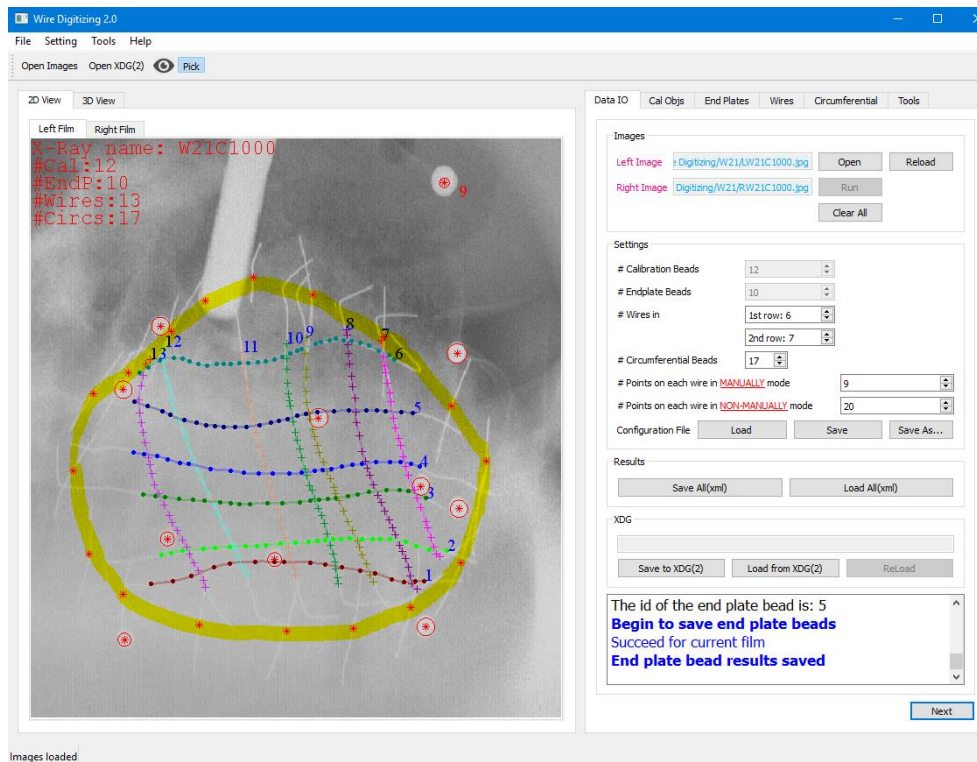
Figure 2.5. *Wire digitizing software environment. Showing the final step of digitizing 10 end plate beads, 13 Wires and 17 highlighted circumferential markers around the disc in left image of specimen W21 after 1000 cycle.*

The software uses all the information from beads and wires within and around the tissue to reconstruct the 3D model of the wire grid using the two following Matlab codes in the current study. By saving all the markers and wires information, it eventually writes the output '.xdg' file format to be used by the next codes (Appendix B).

2.5. Matlab Codes

2.5.1. Reconstruction of wires and points in/around the disc

The original code is written by Ian Stokes in 2004 and 2005 and been modified by John Costi and Zhanheng in 2005 and 2016, respectively, to adapt to the variation of points on the wires instead of nine original number of clicks per wire in previously discussed digitizing software. Further modifications were made in the recent code to fit it to the data by John Costi and the author. This code is using two major functions called 'reconfu' and 'dltfu' using the direct linear transformation (DLT) for the purpose of three-dimensional reconstruction of markers and wires in and around the disc tissue (Costi et al. 2007). This code identifies all the landmarks (calibration points, end plate beads and circumferential markers and wires) separately, for both right and left images and then match them all to reconstruct the final model. The Hungarian method was provided to identify and match the number of ten endplate beads using 'hungarian.m' and 'condass.m' Matlab functions followed by heuristic matching algorithms to identify the rest of landmarks. The best Hungarian matching

set (red circle = 1 or blue square = 2) according to the position of the endplates and the optimum digitizing angle are required to be chosen by the user to minimize the error. Two sets of endplates are suggested by the software based on left or right images as shown in Figure 2.6 from x-y view; knowing that there are 2 sets of endplate beads on each side and the last 2 on top and bottom of the disc where endplate meets the vertebral body, the square option is certainly absurd. The circle is more possible to be the correct position of the endplates; therefore number 1 (circle) is chosen. There is no general rule for choosing the optimum digitizing angle. In this study, the zero angle has been tried first, then it is gradually increased or decreased to positive/negative 60 degrees. All the reading is recorded and analyzed for the purpose of finding the optimum angle with the least bad intersections and the minimum number of outliers. Appendix C represents the optimum angle, Hungarian set and the number of outliers (will be discussed in the following lines) for each specimen.
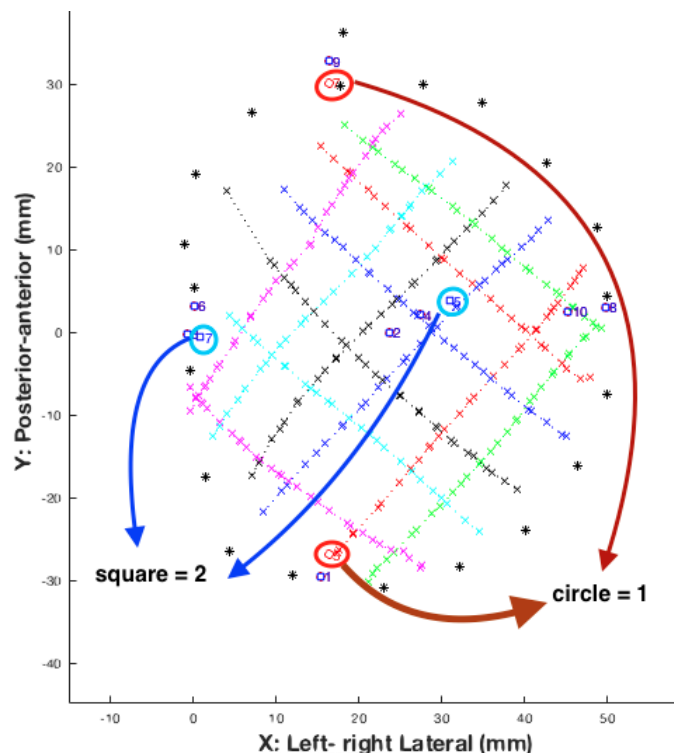
Figure 2.6. Hungarian selection: comparison of two possible Hungarian sets based on the endplate position from X-Y view for specimen number W25; optimum digitizing angle=25 (o = 1; square = 2).

Finally, the three-dimensional model of the wire grid and landmarks is reconstructed as shown in Figure 2.7. Both blue and red circles with the same color crossed line are showing the good or true wire intersection meaning that there is a compromise between left and right images which leads to an acceptable error in the reconstructed image; while, the black crossed line in the middle of the circle (e.g. intersection of wire 1 with wire 7 is marked by a blue circle with the black crossing line) indicates the poor intersection, caused by

disagreement between un-matching left and right images. These poor wire intersections which are known as outliers, were flagged based on the error made by the difference between right and left images and therefore been excluded from the list intersections for further displacement measurements. The poor intersections can be ignored only if they are located outside the wire grid; so, they no longer can cause an error in measuring the displacement of intersections.
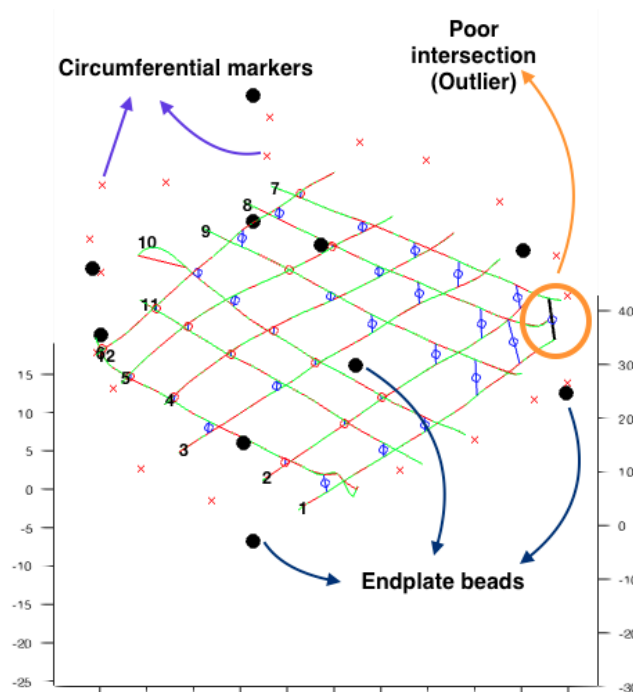
Figure 2.7. The three-dimensional reconstructed wire grid image of specimen W25N (Neutral cycle); choosing optimum angle of 25 and first Hungarian set. Both blue and red circles with the crossed line are showing the true intersection resulted by the strong agreement between left and right images. The intersection between wire 1 and 7 is known as an outlier.

The input of this code is the '.xdg' file written and saved by wire digitizing software and in the end writes different file formats such as '.out', '.log' and '.bad' files for each specimen to be used by sequential codes. The code is converting the digitized beads and wires into intersections which are the basic information of all the following measurements. Therefore, identifying the true wire intersections and outliers is a critical step toward reaching reliable results. Some other spikes other than the ones recognized by the software represents the difference between the digitized wires and the fitted curve. Comparing the effect of removing those poor wire intersections which are not recognized by the software (e.g. intersection of wire 1 and 12 in Figure 2.7) on the final interpolated in the x and y directions, demonstrated the negligible changes in displacements. Based on the measurements, the average displacement caused by removing or keeping this wire intersection is around 0.0393mm in the x-axis and 0.07725mm in the y-axis. Hence, it was decided not to remove any other wire intersections, manually, from the wire grid due to the insignificant changes they made to the final interpolated node positions.

2.5.2. The displacement measurement of intersections

The following code performs the first post-processing step toward measuring the maximum shear strain (MSS) based on the position of the wire intersection in loaded and unloaded reconstructed wire grids. A precise look at Figure 2.8 reveals the minor changes of markers and wires (mm) in and around the disc after 1,000 cycles of combined flexion, axial rotation and compression. Later, a circumferential linear spline fitted poly curve applies to remove the sharp posterior curvature of the disc.

a) Unloaded specimen W16N
(cycle=Neutral)

b) Unloaded specimenW16C1000
(cycle=1000)
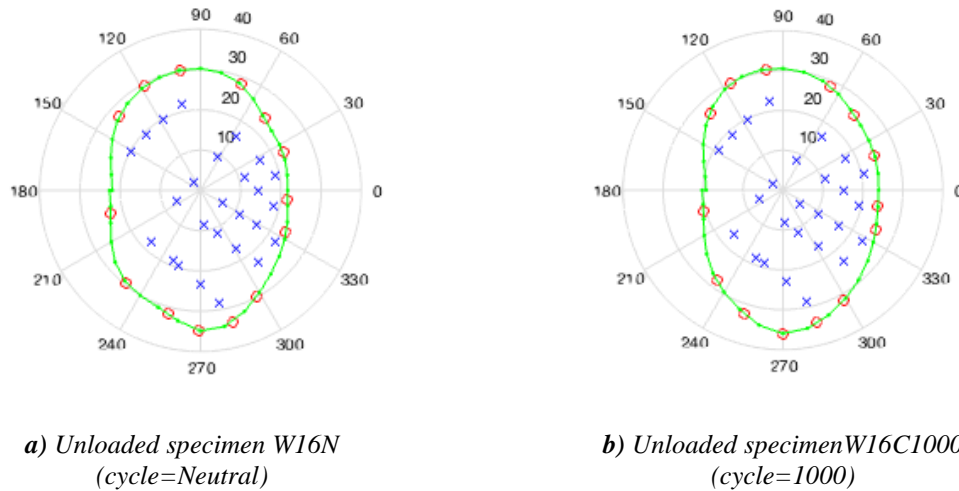
Figure 2.8. *Axial view of plotted landmarks for specimen W16 in both **a**) neutral and **b**) cycle 1000. Red circle= circumferential markers; Blue cross= true intersections; Green line is the fitted spline.*

In addition, comparing the loaded and unloaded reconstructed wire grid, this code excludes outliers from all further strain measurements. Ultimately, using this code, enable us to measure the three-dimensional displacement of each wire intersection, circumferential markers and endplate beads from neutral to the certain cycle of the experiment. Monitoring both magnitude and direction of three-dimensional intra-discal strains in x, y and z coordinates would be useful in understanding the mechanism of the disc deformation under repetitive loading condition; on top of that, the displacements of the endplate and circumferential markers are also important for diagnosing the disc bulge and endplate fractures. Figure 2.9 represents the initial and final position of each of the landmarks from the neutral position to cycle 1000 in specimen W16. The neutral position is considered as baseline, so the instant changes in the tissue displacement vectors are expected to be seen once cycle 1 is applied.
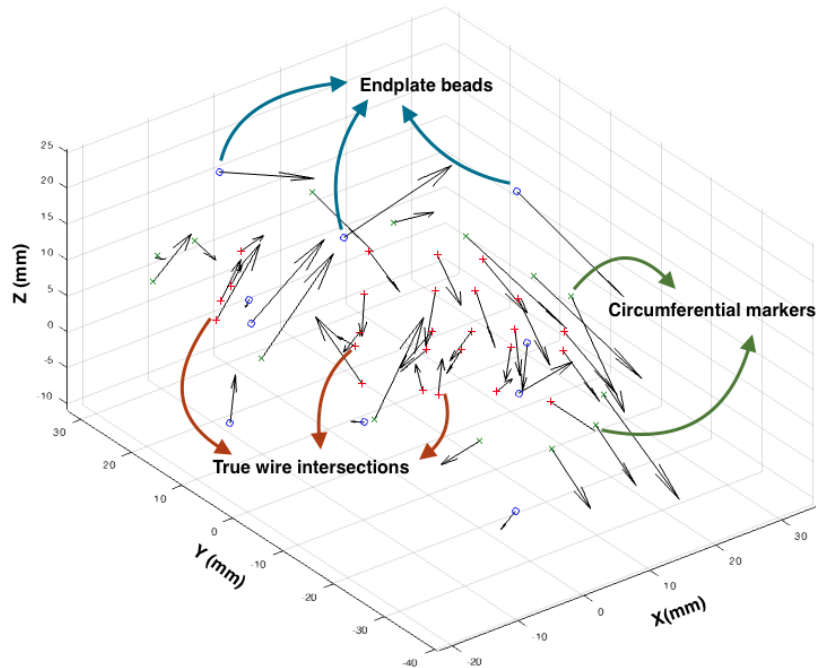
Figure 2.9. *Displacement vectors for specimen W16 cycle 1000 compare to neutral, scaled by a factor of 5. Blue circle= Endplate beads; Red cross= true wire intersection; Green cross= Circumferential markers. Outliers have been excluded in this image to minimize the error (specimen W16 originally had a 5× 6 wire grid which makes the total number of 30 intersections; however, only 26 true intersections are plotted in this image).*

2.5.3. Interpolating the intersections to nodes

Up to this point in this study, the actual wire intersections have been used for tissue displacement measurements. A mathematical technique is being used to interpolate the wire intersections to 173 nodes spread all over the disc (Costi et al. 2007). The Delaunay triangulation is formed based on the position of wire intersections and the circumferential markers, as shown in Figure 2.10. So that the displacement of each node is mathematically computed based on the displacement of the adjacent true wire intersections.
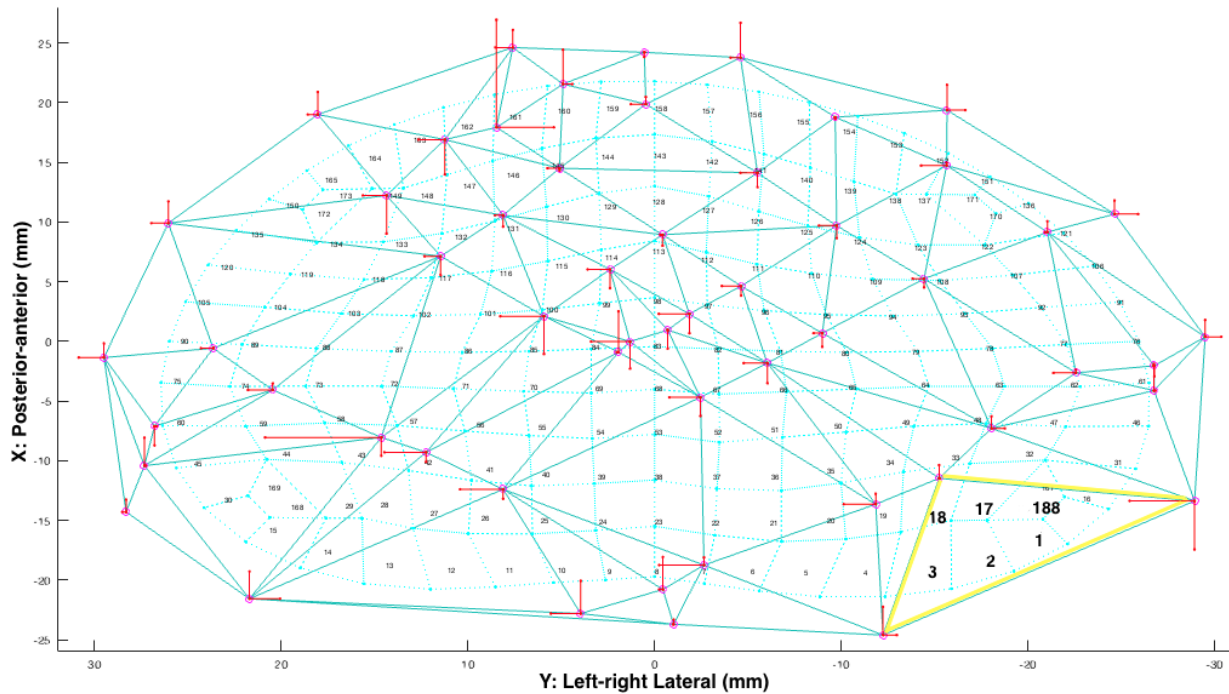
Figure 2.10. *Delaunay triangulation for specimen W12C500 (cycle 500). Nodes number 1,2,3,17,18,188 are receiving the information from three vertices of the highlighted triangle. The pink circles are representing the true wire intersections. So, the continues straight line linking these circles is showing the tantalum wires used in digitizing process.*

Furthermore, A scale factor is required for the new quadrilateral mesh to ensure that the mesh lies within the boundary of the poly fitted curve which determines the periphery of the disc defined by the previous code (see Figure 2.11). In some of the loaded specimens, particularly for the final cycles, a considerable decrease in the scale factor is required, since the disc undergoes an enormous deformation under combined flexion, axial rotation and compression. No change in the scale factor might result in 'NaNs' values in Delaunay and missing parts in largest principle strain (LPS) and MSS colour maps. E.g., the scale factor (originally equals to 0.9) was reduced to 0.85 for specimen W12 cycle 10,000 to adjust the scale within the boundary of the poly fit.
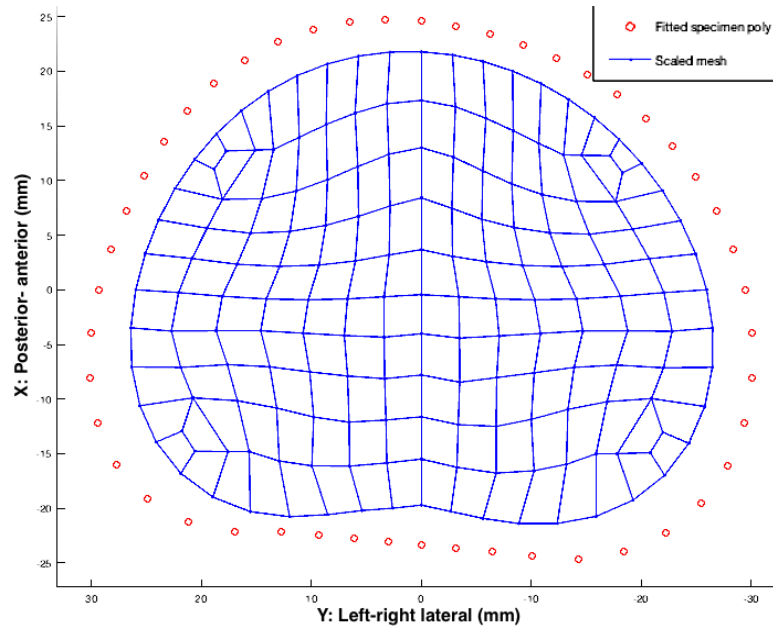
Figure 2.11. *Peripheral fitted poly and scaled quadrilateral mesh for W12 cycle 500 vs neutral.*

It is believed that the largest shear strains are associated with the disc injury under physiological cyclic motions (Costi et al. 2007). The values of tissue displacement, largest principle strain and maximum shear strain are calculated for all 173 nodes in each set of cycles with respect to the neutral position. Therefore, tissue displacement plots are provided to allow scaling of the MSS and LPS contour color maps. As mentioned in the previous section, each group of nodes are receiving the displacement, LPS, MSS values from the nearest intersection points.

2.6. Anatomical regions

In order to evaluate the disc behavior specifically, the tissue is divided into nine separated symmetrical regions as suggested by Costi et al. (2007) defined as Anterior (Ant); Posterior (Post); Left lateral (LLat); Right lateral (RLat); Left Anterolateral (LAntLat); Right Anterolateral (RAntLat); Left posterolateral (LPostLat); Right posterolateral (RPostLat). However, in this study the regions are being stretched inside the disc to include more quadrilateral elements to minimize the error (see Figure 2.12) (Ant= 15 nodes; Post=15 nodes; LLat= 12 nodes; RLa= 12 nodes; LAntLat= 11 nodes; RAntLat= 11 nodes; LPostLat= 14 nodes; RPostLat= 14 nodes); corresponding changes to the code is been made by the author. This study compares the mean of maximum shear strain within regions after the specimen is loaded under certain number of cycles (N, 1, 500,1000,5000,10,000,15,000,20,000) using statistical analysis of variances (ANOVA). The regional division not only allows evaluation of mean MSS and LPS within the anatomical regions but also enables

further comparison of the MRI analysis with the MSS for each region; additionally, it can highlight the region which is experiencing the highest amount of MSS where is possibly the initial failure site in the disc.
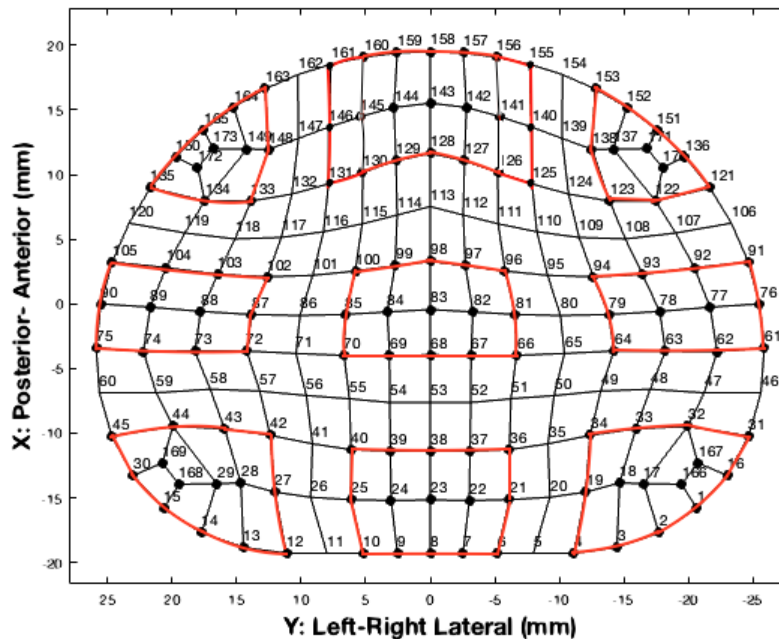
Figure 2.12. *Regional classification of the axial slice of the disc based on the number of nodes included. Each of regions are highlighted by the red line: Anterior (Ant); Posterior (Post); Left lateral (LLat); Right lateral (RLat); Left Anterolateral (LAntLat); Right Anterolateral (RAntLat); Left posterolateral (LPostLat); Right posterolateral (RPostLat).*

2.7. Pre- and Post- MRI Analysis

As mentioned in section 1.5, both pre- and post-failure MRI images in axial and sagittal views are required for the clinical diagnosis of the disc injuries. The observed MRI signal intensity changes may indicate the presence of concentric and radial tears, bone and endplate fractures, bulge and extrusion, deformation of the nucleus bell shape and narrowing in the spinal canal. Particular focus was given to the shape of the spinal canal since the uneven canal could be an indicator of posterior annulus protrusion or nucleus extrusion. All disc abnormalities can be categorized based on their origin; for instance, radial and circumferential tears, and rim lesions all taking place in the annulus which can ultimately form the annular protrusion and disc bulge; furthermore, endplate fracture and nucleus extrusion are initiated from endplate and nucleus, respectively. In addition, the CT scan is provided to inspect the vertebral crush and fractures as well as bony osteophyte (bone spur).

Then, an MRI-based grading system was established by observing the severity of the present radial and circumferential tears in nine regions of the disc discussed in section 2.6. A similar observation- based technique was used by Vernon-Roberts et al. (1997) for macroscopic analyzing and categorizing the disc abnormalities into the following classes such as: radiating and concentric tears, rim lesion and delamination. Although all mentioned abnormalities from the recent study could not be distinguished using MRI image, same disc

abnormalities subcategories were used to evaluate and score the level of disc damage from 0 to 3 interpreting as no change, low, moderate and severe changes, respectively. For a better comparison, MRI images are all flipped horizontally to match the right and left lateral interpolated model in MSS analysis. However, MRI analysis is subjective and therefore non-reproducible. The MRI scores and data analysis have been assigned by the author and then in order to avoid the misinterpreting of MRI signal changes due to lack of skill and experience in detecting visual errors in grading the tissue damage, assistance from Dhara Amin has been sought in current study.

Finally, findings from MSS and MRI analyses are compared and the Spearman correlation factor will be calculated to interpret the strength and direction of the relationship between these two methodologies.
It is expected that the variation of maximum shear strain magnitudes could be explicated by the clinical analysis of MRI images; also, findings from these two methods would be supported by the visual observation of the tissue damage.

Chapter 3: Results

One of the specimens (W21) was excluded from the final analysis due to the enormous error in 500th cycle caused by digitizing complexities; therefore, the sample size has reduced to 7 (N=7).

3.1. Individual tissue displacement

Figure 3.1. demonstrates the three-dimensional displacement magnitude and direction of one of the specimens after 500 cycles in the x-y plane. Dividing the disc into four regions (left posterior (red), right posterior (purple), left anterior (green) and right anterior (blue)) enables a better visualization of the disc deformation. The red-dotted disc demonstrates the final position of the disc after cycle 500th; while the black line is showing the neutral position of the disc. As expected the disc tissue would move towards the right anterolateral side under the forward flexion, right axial rotation and compression (Figure 3.1.a). It can be inferred from the side view (Figure 3.1.b) that the anterior region is experiencing higher displacement (up to 4.5 mm along the z axis) compare to the posterior (up to 2.75 mm); which can be justified knowing that forward flexion is applied on the disc tissue. Lateral view (Figure 3.1.c) also reveals the higher displacement of the left and right anterior regions (negative z values) compare to the posterior (blue/green vectors vs. purple/red). Moreover, the highest amount of tissue displacement is taking place somewhere between left and right anterior regions which can be also seen from the axial view (Figure 3.1.a).

a) Axial view.

b) Side view (posterior-anterior).

c) Lateral view.
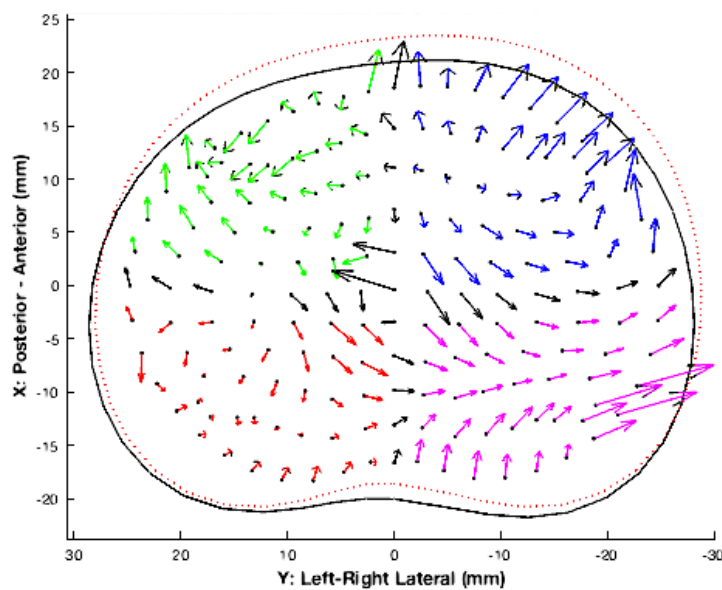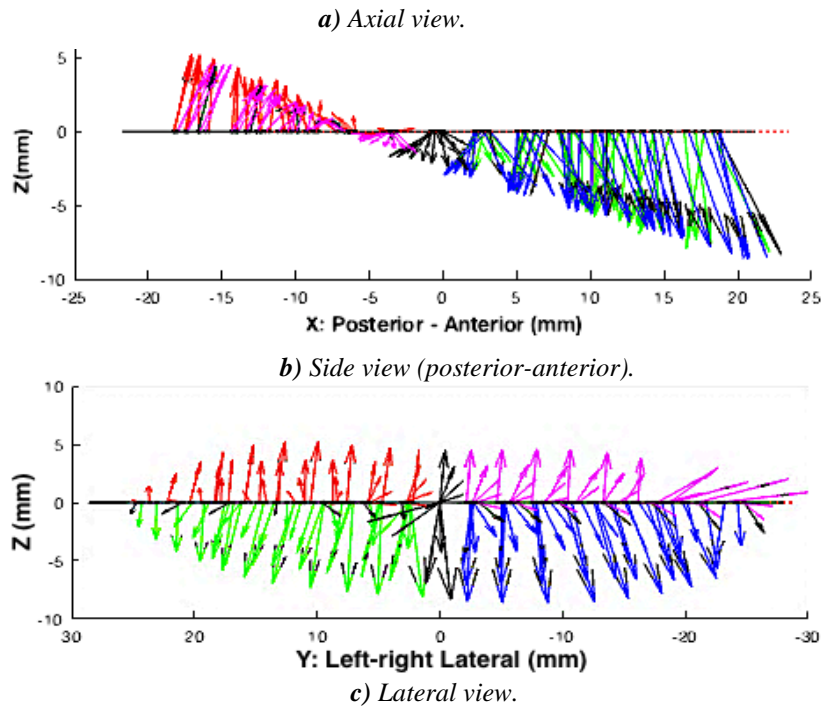
Figure 3.1. *Different views of the internal disc displacement vectors in four regions (left posterior (red), right posterior (purple), left anterior (green) and right anterior (blue) for specimen W16 (cycle 500) under combined forward flexion, right axial rotation and compression; magnified 2X.* ***a)*** *Axial view* ***b)*** *side view (posterior-anterior)* ***c)*** *Lateral view.*

3.2. Individual LPS and MSS

Both MSS and LPS were calculated and normalized based on the neutral position; contour color plots offer a better visual comparison of the tissue (Figure 3.2). According to Figure 3.2, the left lateral and left posterolateral regions are experiencing the highest amount of LPS tension (yellow= +60%) and compression (dark blue= -30%) as colored by the extreme positive and negative ends of the color bar.
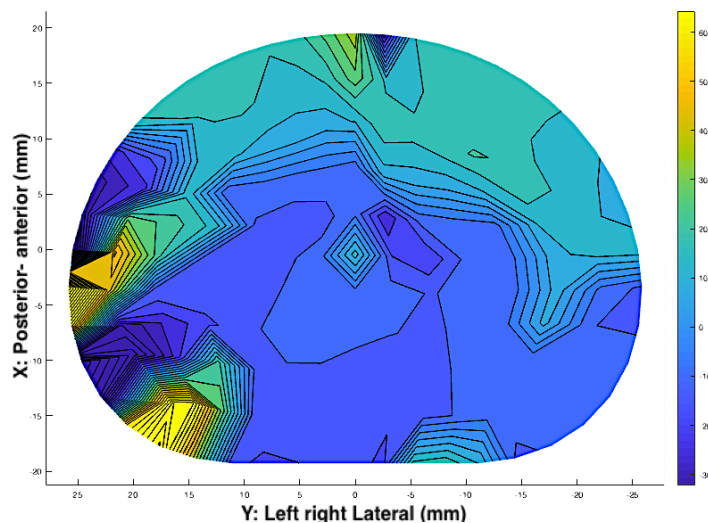
Figure 3.2. *Largest Principle Strain contour map for specimen W25 (Cycle 500 compared to neutral) under combined forward flexion, right axial rotation and compression; The largest magnitude of Principle strain is taking place in the left lateral and left posterolateral regions of the disc. The two extreme ends of LPS color bar are interpreted as tension (yellow, positive 60%) and compression (dark blue, negative 30%).*

The MSS contour color plot also suggests the same (Figure 3.3), as left posterolateral demonstrates the highest MSS (roughly around 70-80%) while anterior is possibly the second highest amount of MSS which can be confirmed by LPS analysis from Figure 3.2. Analyzing the intradiscal MSS and LPS color plots implies that the same region of the disc is experiencing the highest MSS and also the largest magnitude of principle strain where the tissue undergoes a massive deformation.
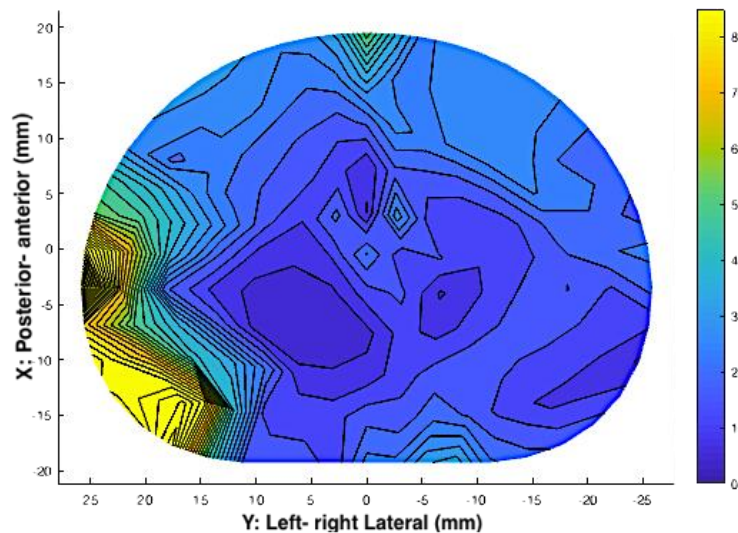
Figure 3.3. Maximum Shear Strain contour map for specimen W25 (Cycle 500 compared to neutral); The largest MSS is taking place in the left lateral and left posterolateral regions of the disc (80%/mm) where the highest LPS is taking place.

3.3. Tissue displacement progression

This study enabled monitoring the tissue displacement and deformation over time for each individual specimen (see Figure 3.4) as well as for average of all seven specimens (Figure 3.5) which can be helpful to understand the mechanism of the disc deformation up to failure. The progressive graphs in Figure 3.4 demonstrate the disc displacements of specimen W18 from cycle 1 to cycle 10,000. Displacements were calculated based on the neutral position for each of the cycle sequences to allow the comparison over time. It can be seen that the magnitude of the displacement vectors increases as the experiment proceeds to the final cycle (10,000 for this particular specimen). As expected the disc tissue move towards the right anterolateral trajectory of the x-y plane from the first cycle since the right axial rotation is being applied to the disc.

a) Cycle 1   *b) Cycle 500*   *c) Cycle 1000*

d) Cycle 5,000   *e) Cycle 10,000*
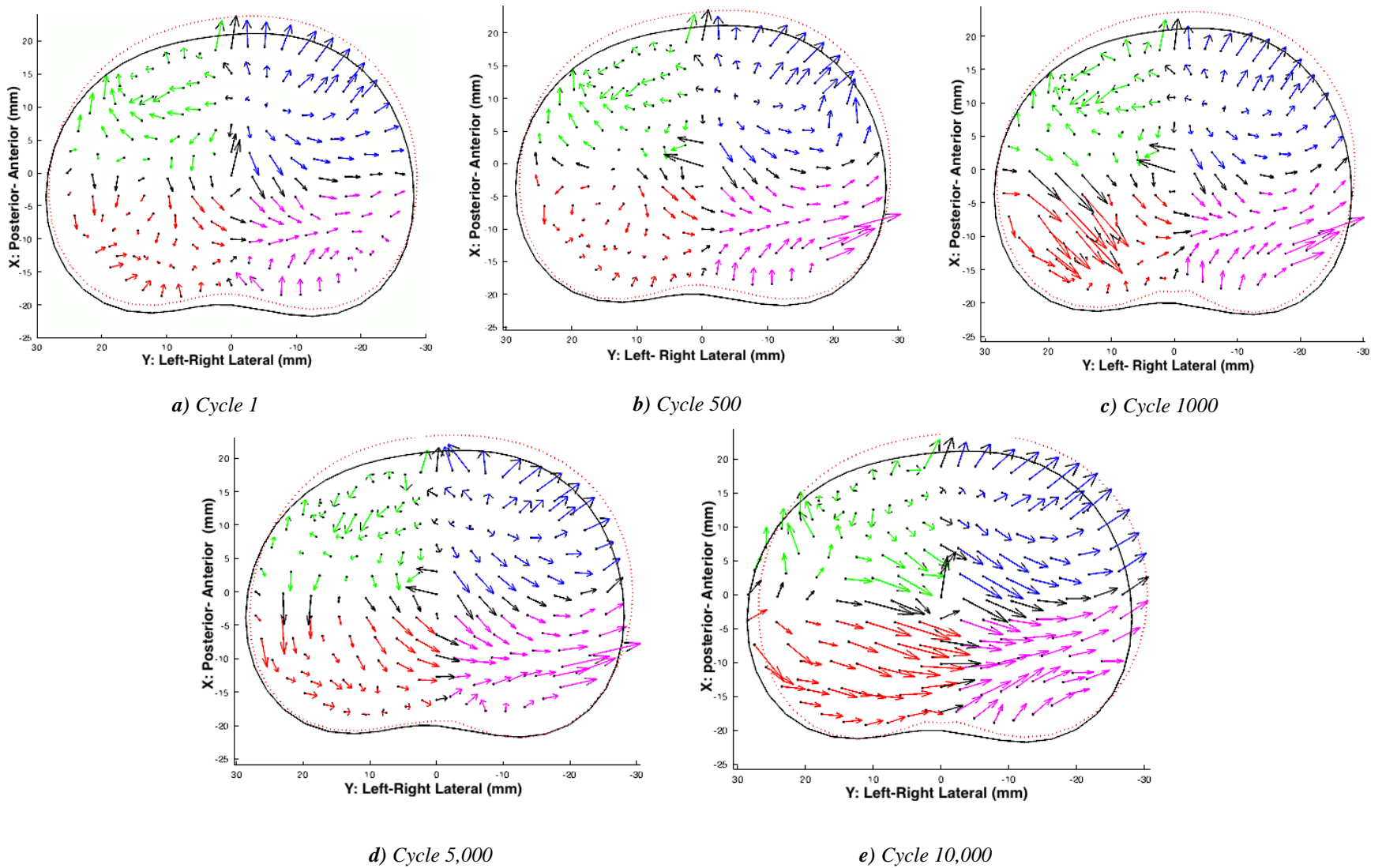
Figure 3.4. *Monitoring the three-dimensional disc displacement progression in specimen W18 at certain intervals up to 10,000 cycles.*

Plotting the mean displacement, LPS and MSS for each individual specimen as well as for all the specimens could be useful in terms of understanding the graduate movement of the disc tissue under particular loading scenario. The image below represents the average displacements of all the specimens from cycle one to 10,000 under combined flexion, right axial rotation and compression.

a) Cycle 1   *b) Cycle 500*   *c) Cycle 1000*

d) Cycle 5,000   *e) Cycle 10,000*
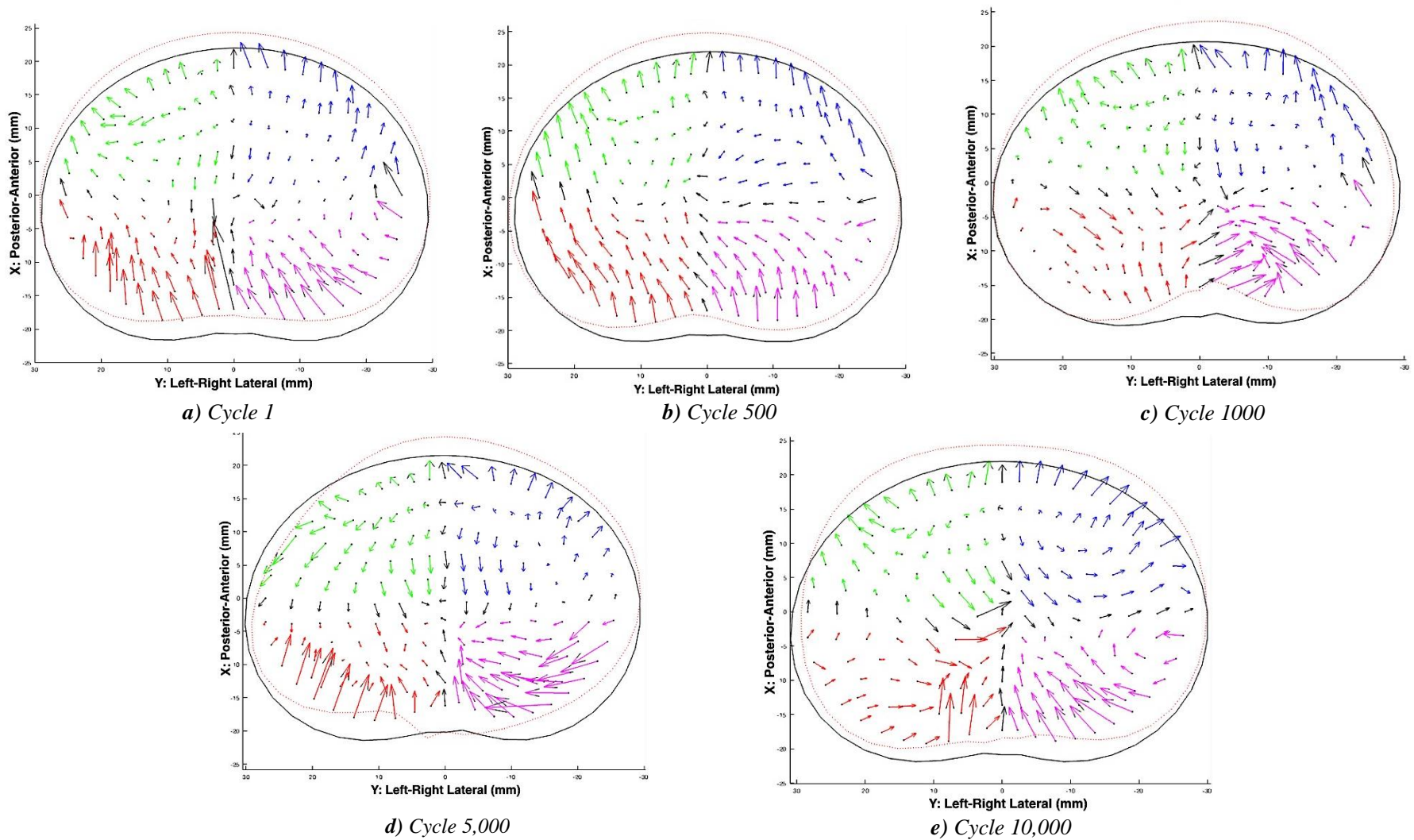
Figure 3.5. *Average mean tissue displacement of all seven specimens over 10,000 cycles. X: Posterior-Anterior (mm) Y: Left- Right Lateral (mm).*

3.4. Displacement, largest principle strain and maximum shear strain

The mean, standard deviation (SD) and 95% confidence intervals (95% CI) of the tissue displacement have been provided along the x, y and z-axes for all the specimens in all nine regions. Table 3.1 is representing the tissue displacement, LPS and MSS for one of the specimens at its final cycle (10,000[th] cycle). A brief overview of the mean displacement values across the regions only in one direction indicates the minimum 0.13 mm (corresponds to the annulus and anterior in x and y directions, respectively) and maximum 3.59 mm (corresponds to right posterolateral in z-axis followed by 3.41 mm displacement in posterior) of tissue displacement. The minimum and maximum of largest principle strain (%) were also reported as -52 and 38, respectively. Last but not least, MSS values vary in the range of 30-87%, across regions. The highest amount of MSS is taking place in the nucleus where the minimum largest principle is acting (-0.52%) while the lowest MSS corresponds to the left lateral region. Appendix D is providing the tissue displacement, largest principle strain and maximum shear strain values of the final cycle for all seven specimens in this study.

Table 3.1. *Tissue displacement, largest principle strain(LPS) and maximum shear strain (MSS) readings for specimen W12 final cycle (Cycle 10,000); Anterior (Ant); Posterior (Post); Left lateral (LLat); Right Lateral (RLat); Left Anterolateral (LAntLat); Right Anterolateral (RAntLat); Left Posterolateral (LPostLat); Right Posterolateral (RPostLat); Nuc (Nucleus). SD= standard deviation 95CI= 95% confidence interval.*

Region	Displacement (mm)									Largest Principle Strain (%)			Maximum Shear Strain (%)		
	Mean			SD			95% CI								
	dx	dy	dz	dx	dy	dz	dx	dy	dz	mean	sd	95ci	mean	sd	95ci
Ant	0.2239	0.1315	-1.9463	1.3698	0.5283	0.6741	0.6932	0.2673	0.3411	35.74	17.26	8.74	55.17	21.11	10.68
Post	0.7072	-1.6553	3.4177	0.8480	0.4867	0.5783	0.4291	0.2463	0.2927	36.20	7.02	3.55	60.58	15.40	7.80
LAntL	-0.5386	0.6439	-1.5965	0.8944	0.2194	0.4935	0.5285	0.1297	0.2916	-23.75	5.95	3.52	46.22	15.14	8.95
RAntL	0.7404	-0.7105	-0.8310	0.4462	0.4414	0.5113	0.2637	0.2609	0.3022	-23.59	1.769	10.46	37.97	23.53	13.90
LLat	0.9092	-0.4067	0.4499	0.7399	0.3915	0.4525	0.4186	0.2215	0.2560	17.03	1.059	5.99	30.45	9.46	5.35
RLat	0.4621	-0.8630	1.2664	0.7731	1.8415	0.4619	0.4374	1.0419	0.2613	-39.62	5.182	29.32	58.78	54.82	31.02
LPosL	0.9792	-1.8179	2.7972	0.6297	0.6864	0.6305	0.3298	0.3595	0.3303	29.34	7.64	4.00	54.92	12.17	6.37
RPosL	0.4066	-0.2768	3.5902	1.3648	1.2820	0.5891	0.7149	0.6715	0.3086	38.85	6.36	3.33	76.08	17.63	9.24
Nuc	-0.1372	-2.0103	0.8813	2.4822	2.4306	0.5145	1.2562	1.2301	0.2604	-52.21	51.40	26.01	87.01	66.40	33.60

3.5. Statistical analysis

3.5.1 Average regional Maximum Shear Strain and Largest principle strain

The mean (SD) regional maximum shear strain (%) was also calculated for all the specimens after a certain number of cycles (500 cycles) (Figure 3.6). Cycle 500 was chosen since it contains all seven specimens in comparison to other sequences (cycles 1,000 and 5,000 (N=5), cycle 1,000 (N=4) and cycles 15,000 and 20,000 (N=1)).

a) Mean (SD) % maximum shear strain   *b) Mean (SD) Largest % Principle strain*
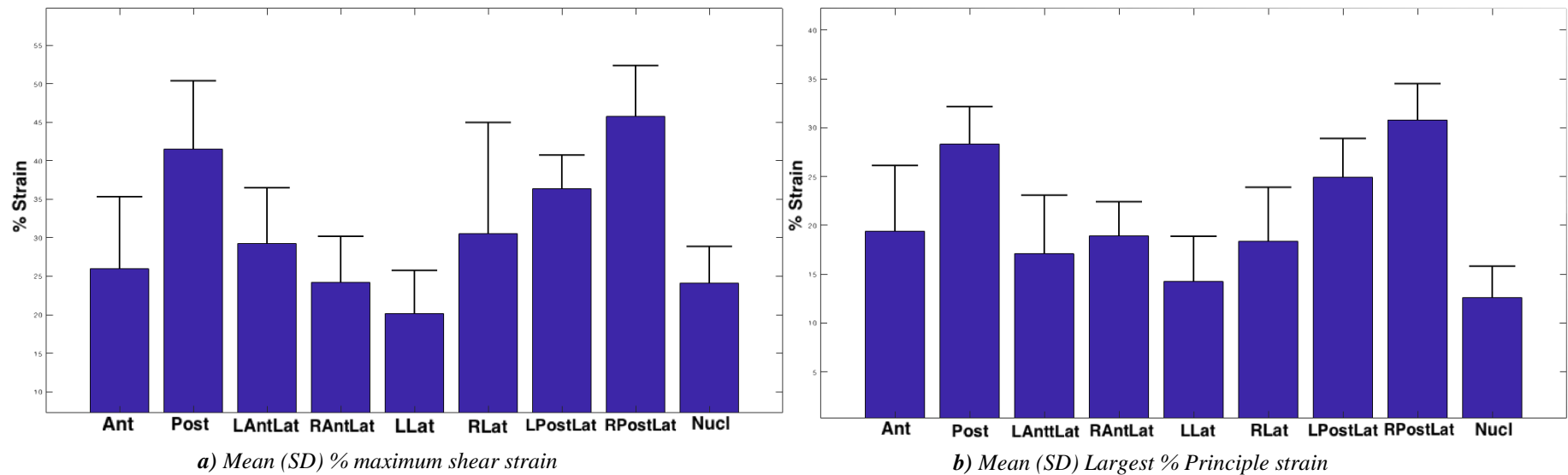
Figure 3.6. *Average regional distribution of MSS and LPS after 500 cycles of combined forward flexion, right axial rotation and compression; Anterior (Ant); Posterior (Post); Left lateral (LLat); Right lateral (RLat); Left Anterolateral (LAntLat); Right Anterolateral (RAntLat); Left posterolateral (LPostLat); Right posterolateral (RPostLat).*

The SPSS software was used to compare the mean values of maximum shear strain (%) in nine anatomical regions of the disc at 500 intervals in all seven specimen. Obviously, the null hypothesis (which is the absence of meaningful relationship between MSS and MRI scores) is rejected, since the various mean of maximum shear strain has been observed within each of the nine locations and there are no regions reported to take the same value of the mean maximum shear strain. Statistical analysis is required to be able to discuss the MSS and LPS differences within regions quantitatively. According to Table 3.2, the highest mean MSS associates to the right posterolateral region (62.4%) with the standard deviation of 33.4 % within the total number of 98 nodes which is followed by the minimum mean MSS under combined flexion, right axial rotation and compression (Table 3.2).

Table 3.2. The SPSS analysis of mean of MSS (dependent variable) over nine anatomical regions (fixed factor)I at the final cycle. N= total number of nodes per region across all the specimens.

Disc Region	Mean	Std. Deviation	N
Anterior	38.8901	20.25619	147
Posterior	57.1295	32.03788	105
Left Anterolateral	46.0581	17.03788	77
Right Anterolateral	42.4006	30.30558	77
Left Lateral	40.6418	22.76138	84
Right Lateral	46.6938	52.78397	84
Left Posterolateral	59.0826	21.97768	98
Right Posterolateral	62.4169	33.41840	98
Nucleus	44.3755	21.53771	105
Total	48.4907	30.21875	875

Plotting the data obtained from table 3.2 exhibits the mean values of MSS in nine regions across all seven specimens (Figure 3.7). It also confirms the maximum and minimum values of mean MSS in right posterolateral and anterior, respectively, as previously stated.
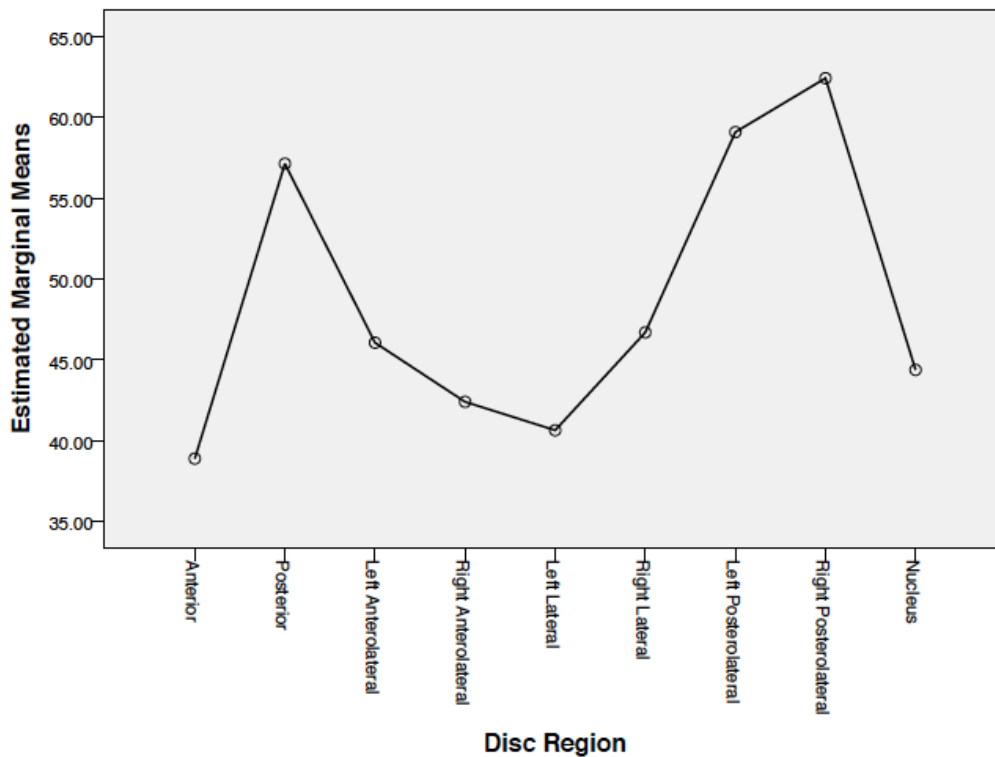
Figure 3.7. The estimated marginal means of maximum shear strain (%) extracted from the final cycle in all seven specimens (W12, 13, 15, 16, 18, 23, 25) over nine regions. The right posterolateral region is experiencing the highest mean MSS under flexion, axial rotation and compression followed by left posterolateral and posterior.

3.5.2. The effect of regions on MSS across all the specimens

Running the SPSS software for the entire dataset of 875 (N=875) from all nine anatomical regions (i.e. resulted in the number of specimens times the number of nodes per each region) demonstrates that the effect of regions overall is highly significant (P<0.001).

According to Appendix E, there are significant differences between anterior with posterior, left posterolateral and right posterolateral. Also, the right posterolateral region is significantly different to posterior, left posterolateral and right posterolateral. The effect of the nucleus is usually been reported since it is known to undergo the least deformation compare to the other regions. Therefore, Table 3.3 is showing the difference of nucleus values with all other regions. The effect of the nucleus is marginally not significant (P=0.057), however, of the effect of the nucleus is significant on left posterolateral and right posterolateral (P=0.013 and P=0.000, respectively).

Table 3.3. The effect of regions on each other; The significant difference between regions are been marked with starts in Mean difference column (dependent variable= maximum shear strain; anatomical regions= fixed variable).

(I) Disc Region	(J) Disc Region	Mean Difference (I-J)	Std. Error	Sig.[b]	95% Confidence [b] Lower Bound
	Left Anterolateral	16.359*	4.440	.009	2.118
	Right Anterolateral	20.016*	4.440	.000	5.775
	Left Lateral	21.775*	4.335	.000	7.870
	Right Lateral	15.723*	4.335	.011	1.818
	Left Posterolateral	3.334	4.165	1.000	-10.025
	Nucleus	18.041*	4.095	.000	4.907
Nucleus	Anterior	5.485	3.725	1.000	-6.463
	Posterior	-12.754	4.024	.057	-25.660
	Left Anterolateral	-1.683	4.375	1.000	-15.713
	Right Anterolateral	1.975	4.375	1.000	-12.056
	Left Lateral	3.734	4.268	1.000	-9.955
	Right Lateral	-2.318	4.268	1.000	-16.007
	Left Posterolateral	-14.707*	4.095	.013	-27.842
	Right Posterolateral	-18.041*	4.095	.000	-31.176

3.6. MRI Analysis

Table 3.4 summarizes the MRI analysis of the specimens based on visual examination of pre- and post-MRI images (see Appendix F). The annular protrusion and disc bulge were observed in five out of seven specimens; there was only one case of nucleus extrusion and one endplate fracture. Vertebrae crush fracture also was observed in one specimen (W25) using the CT-scan, which has probably occurred due to the poor bone quality of the cadaver. It can be inferred from Table 3.4 that the circumferential tears are the most common type of disc damage; also, the annulus pulpous seems to be the initial site for disc failure in the majority of the specimens under combined flexion, axial rotation and compression. Then, the grading system discussed in section 2.7 was used to evaluate the tissue damage in nine regions of the disc.

Table 3.4. MRI-based observations in disc regions and the possible mode of failure.

Specimen ID	Observations	Disc region	Possible mode of failure
W12	Circumferential tears, anterior separation and tissue lost, uneven spinal canal	Right posterolateral, nucleus and anterior	Annular protrusion (disc bulge)
W13	Fracture, circumferential tear	Superior endplate fracture, right lateral, posterior, nucleus	End plate fracture
W15	Concentric tear, tissue lost anteriorly, annulus darker than middle, disparity	Posterior, inferior endplate, posterolateral annulus separation	Annular protrusion, endplate fracture, disc bulge
W16	Circumferential tears	Posterior, right anterolateral	Annular protrusion
W18	Circumferential tears, extrusion, bulge	Right anterolateral, nucleus	Nucleus extrusion (disc prolapse), Posterior bulge
W23	Spinal canal blockage	Right posterolateral, posterior, nucleus	Annular protrusion
W25	Bone fracture	Left posterolateral	Vertebral crush fracture, Annular protrusion

3.7. Correlation between regional MRI grades and MSS scores

The tissue damage was investigated for each specimen based on the pre- and post- MRI in both axial and sagittal views. So, the pre-MRI image needs to be compared with the MSS color map in the first cycle; while the post-MRI corresponds to either the final or failure cycle. Table 3.5 demonstrates the correlation between MRI and MSS scores; however, the two analyses are diverse, in nature. There is usually more than one region with grade three (interpreted as severe damage) suggested by MRI analysis since in the final cycle the disc is experiencing a massive amount of deformations and therefore changes in signal intensity, however, reporting two regions with an identical maximum shear strain is quite unlikely in MSS analysis.

Table 3.5. MRI and the MSS analyses comparison table in 9 regions for all seven specimens. Anterior (Ant); Posterior (Post); Left lateral (LLat); Right lateral (RLat); Left Anterolateral (LAntLat); Right Anterolateral (RAntLat); Left posterolateral (LPostLat); Right posterolateral (RPostLat).

Specimen ID	Methods																	
	MRI Analysis									MSS Analysis								
	Ant	Post	LAntL	RAntL	LLat	RLat	LPosL	RPosL	Nuc	Ant	Post	LAntL	RAntL	LLat	RLat	LPosL	RPosL	Nuc
W12	3	3	1	1	1	2	3	3	3	0.5517	0.6058	0.4622	0.3797	0.3045	0.5878	0.5492	0.7608	0.8701
W13	1	3	1	0	1	3	1	2	1	0.4573	0.8843	0.6435	0.3326	0.3642	1.2896	0.627	1.2408	0.5835
W15	3	3	2	2	1	1	2	3	1	0.9521	1.0448	0.8826	0.9013	0.6334	0.5781	0.701	0.9699	0.4313
W16	3	3	3	3	1	2	1	2	1	0.4485	0.3315	0.4053	0.3869	0.2218	0.2309	0.2011	0.3248	0.276
W18	3	1	1	3	1	2	1	1	3	0.7031	0.4077	0.3839	0.7914	0.4846	0.348	0.314	0.2715	0.592
W23	1	3	1	1	1	2	2	3	3	0.3512	2.6614	0.3912	0.3138	0.2153	0.4079	0.1715	1.604	0.9565
W25	2	1	2	1	3	1	3	1	1	0.2801	0.167	0.2852	0.2591	0.5503	0.1833	0.6819	0.1511	0.1336

The Spearman Correlation factor was used in this study to measure the strength and direction of the relationship between two datasets obtained from MRI and MSS analyses. This method is used to correlate the categorical MRI scores (0-3 based on the signal intensity changes) to the numerical maximum shear strain values (%) over nine anatomical regions. Two-tailed P values were also reported to evaluate the probability of the null hypothesis. Table 3.5 represents the magnitude of tissue vector, largest principle strain and maximum shear strain for specimen W12 at the final cycle (10,000); from here, the correlation between MRI and MSS scores can be calculated using R statistical software. The magnitude of displacement vector can be obtained for each region using the square root of mean displacement in x, y and z-axes from Table 3.1. Considering the value of MSS, it can be inferred

that the highest MSS (87.01%) is where nucleus takes place and second highest MSS (76.08%) is associated with the right posterolateral (RPosL) circumferential tears which are the two locations with severe damage addressed by the MRI analysis (Table 3.6). Correspondingly, the nucleus seems to have the highest deformation among all the regions, therefore, it is also associated with the highest amount of largest principle strain equals to -52.21% (the negative LPS indicates the strains under compression).

Table 3.6. *The tissue displacement, largest principle strain, maximum shear strain and MRI score in 9 regions for specimen W12-final cycle: 10,000. Disc region undergoing the highest MSS is highlighted.*

Regions	Tissue displacement (mm)	Largest Principle Strain (%)	Maximum Shear Strain (%)	MRI Score
Ant	1.9567	35.74	55.17	3
Post	3.8523	36.20	60.58	3
LAntL	1.7951	-23.75	46.22	1
RAntL	1.3198	-23.59	37.97	1
LLat	1.0888	17.03	30.45	1
RLat	1.5981	-39.62	58.78	2
LPosL	3.4724	29.34	54.92	3
RPosL	3.5338	38.85	76.08	3
Nuc	2.1992	-52.21	87.01	3

Therefore, the Spearman correlation factor equals to 0.78 for specimen W12 (final cycle) and the two-tailed value of P is less than 0.01 using R software. Conclusively, the association between the MSS and MRI values would be considered statistically significant. Moreover, the Spearman correlation factor for LPS and MSS values is 0.08 with the two-tailed P value of 0.83 which also demonstrates the strong relationship between these two strain values. In addition, tissue displacement and MRI score are strongly correlated with the factor of 0.85 and the 0.003 P two-tailed value which provides enough evidence to reject the null hypothesis. Appendix D is showing the tissue displacement, LPS and MSS, as well as MRI score for the rest of the dataset (specimen number W13, W15, W16, W18, W23, W25) to investigate the correlation factor in each individual specimen aside from the entire dataset (see Table 3.7). Accordingly, the correlation factor for all seven specimens in this study is 0.59 which is still statistically significant; two-tailed P value is reported to be negligible for the whole data (Table 3.7) (P<0.001).

Table 3.7. *Spearman correlation factor and two-tailed P value for each individual specimen as well as the entire dataset.*

Specimen ID	Spearman Correlation Factor	Two-tailed P value
W12	0.78262	0.01265
W13	0.80678	0.00859
W15	0.9486	0.0001
W16	0.89087	0.00127
W18	0.72672	0.02656
W23	0.7216	0.02819
W25	0.9037	0.00083
Total	0.59666	0.00000025

Chapter 4: Discussion

4.1. Overview

Obtaining a significant agreement between MSS and MRI analyses was the primary objective of the current study, which was successfully achieved. The concentration of MSS values in the annulus is associated with tears and fractures in posterior and posterolateral regions of the disc. In addition, the current study suggests the common pertinent sites of failure corresponding to the combined axial rotation protocol of loading to be the posterior and posterolateral regions of the disc. This study also found several distinct modes of disc failure such as annulus protrusion (in specimens W12, 15, 16, 23, 25) nucleus extrusion (W18) and endplate fracture (W13), bone crush fracture (W25). Recent findings from the current study correspond to few other studies (Adams et al. 1994; Callaghan & McGill 2001; Wade et al. 2014) although using dissimilar loading scenarios and motions, they all address annulus as the initial failure site with the highest MSS (%) under combined loading conditions. It is possible that the disc develops the circumferential tears in lamellae layers under combined loading scenarios which result in disc prolapse. Finally, according to section 3.5.1 for the average of the specimens, the right posterolateral region of the disc is reported to experience the highest magnitude of mean MSS (%) among nine anatomical regions under the forward flexion, right axial rotation and compression.

4.2. Comparison to other studies

4.2.1. Experimental study

Results from this study are consistent with the findings from an experimental study conducted by Costi et al (2009) which has addressed the common failure disc regions at the highest risk of injury under certain motions. According to Figure 4.1, the anterior and left posterolateral regions are experiencing the highest risk of the injury associated with the highest maximum shear strain under isolated flexion and left axial rotation, respectively. Therefore, it can be inferred that the posterior region is the common site of failure under combined flexion and axial rotation. Similarly, findings from Figure 4.1 suggests that isolated lateral bending is relatively safe which has also approved by Schmidt et al. (2007) reported to be experience the lowest intradiscal pressure under pure lateral bending.
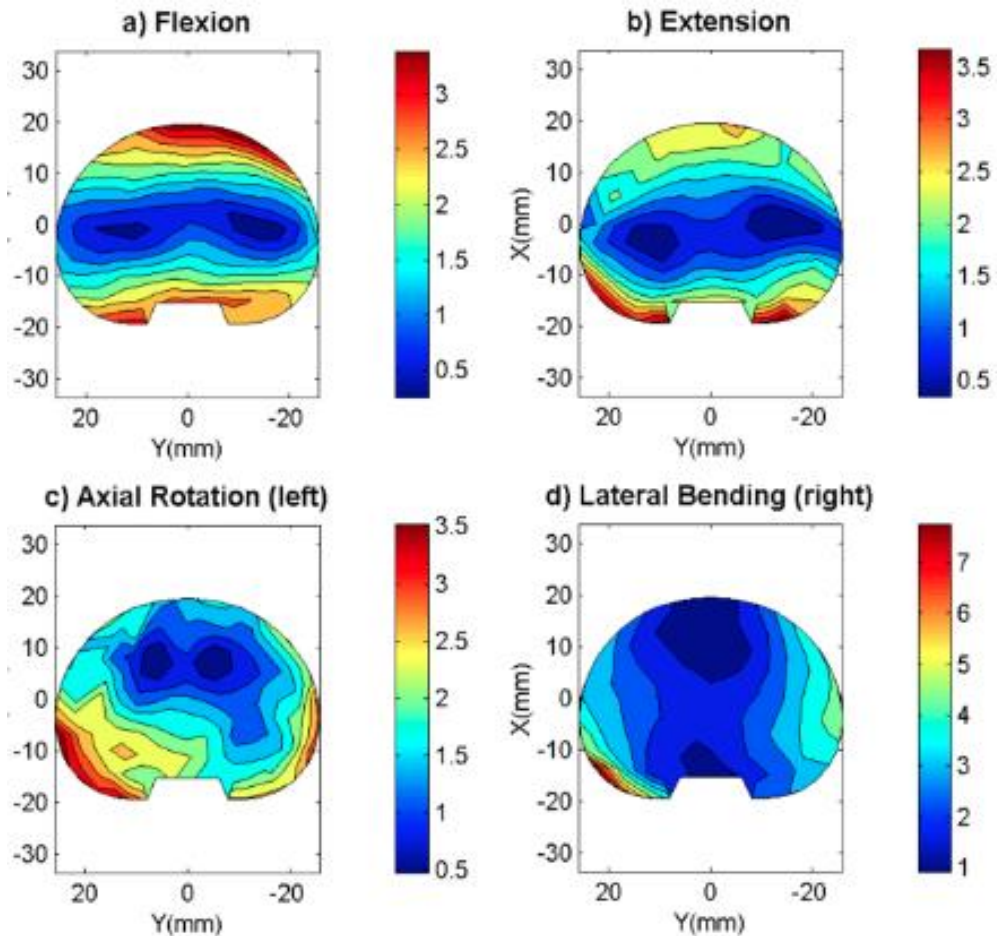
Figure 4.1. *Disc regions are showing the highest MSS under isolated loading scenarios: flexion(**a**), extension(**b**), axial rotation (**c**), lateral bending (**d**). The left posterolateral region experiences the highest amount of MSS under isolated left axial rotation; Anterior and posterior regions are representing the highest MSS under isolated flexion; lateral bending (right) is fairly safe motion since it does not cause large MSS within the disc (Costi et al. 2009).*

The same study has reported the largest maximum shear strain is happening in both anterior and posterolateral regions under combined compression (0.6mm), flexion (13 degrees) and 3 degrees of axial rotation (see Figure 4.2). Although the previous Figure is showing that the pure left axial rotation causes the highest MSS in the left posterolateral region; the combined flexion, right axial rotation and compression is suggesting that the opposite posterolateral side (left posterolateral region) is undergoing the highest MSS after anterior and right anterolateral regions. Findings from this study lines up with the first possibility (isolated left axial rotation), as the right posterolateral region experiences the highest MSS under combined flexion, right axial rotation and compression (section 3.5.1). In addition, the largest MSS has reported as 50% which is very close to findings from this study (62%). Using considerably different loading conditions would be the reason behind diverse results since this study designed to apply flexion (13 degrees), right axial rotation (2 degrees) and 1.7 MPa compression.
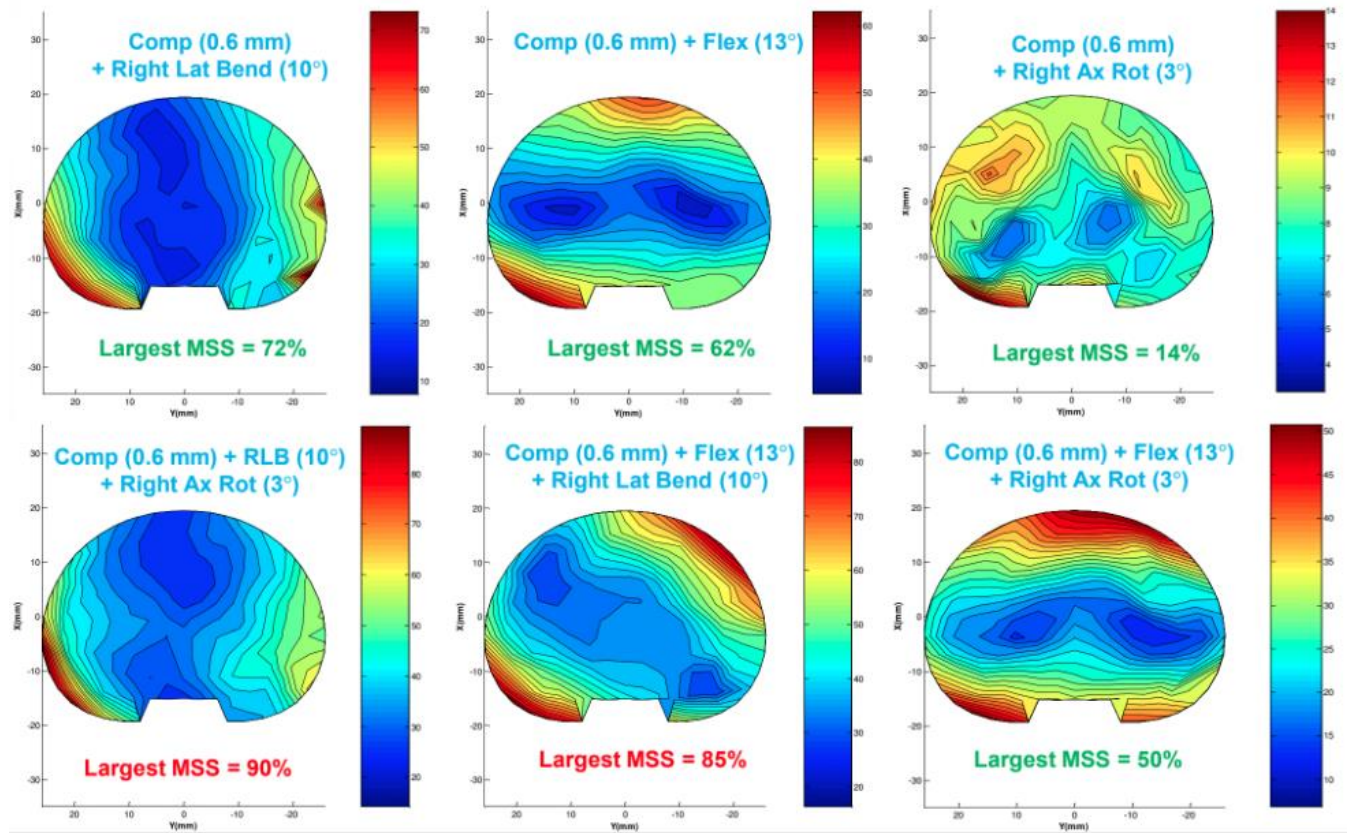
Figure 4.2. *Contour color maps showing the disc regions undergoing the highest MSS (%) under combined loading scenarios (Costi et al. 2009). Anterior and posterolateral regions had reported with the highest MSS (around 50%) under combined compression (0.6mm), flexion (13 degrees) and 3 degrees of axial rotation.*

4.2.2. Computational study

A study by Schmidt et al. (2007) developed a three-dimensional FEA model of L4-L5 to investigate the internal strains within the annulus layers under various loading scenarios. Schmidt et al. have also addressed the posterolateral annulus regions and inferior endplate junction with the highest MSS within the disc for the combination of axial rotation and flexion, respectively (Figure 4.3).

43

a) Maximum shear strain | *b) Maximum fiber strain*

Grade 0 —— Grade 1 —— Grade 2 —— Grade 3
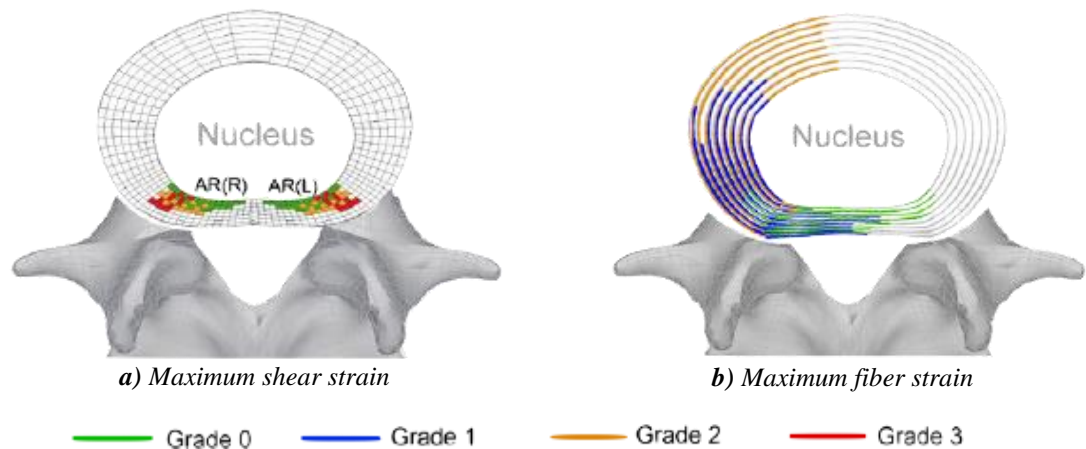
Figure4.3. *The predicted annulus locations experiencing 90% larger than peak shear and fibre strain, under right axial rotation (AR(L)) plus flexion in relevant to the disc degeneration grade (0-3) (Schmids et al.2007). a) The left posterolateral mid-annulus is experiencing the highest MSS in grade 2 degenerated discs (Schmids et al.2007). b) The lateral and posterolateral annulus fibres are experiencing the strain larger amount of strain than 90% of the peak value in grade 2 degenerated discs (Schmids et al.2007).*

4.3. Limitations

The following complexities were presents in the current study. Apart from the macroscopic analysis which unfortunately could not be performed due to the time limitation of the masters candidature, the designated methodology itself has a couple of complexities regarding the digitizing process. As mentioned in section 2.1, the wires and markers are not always recognizable in the x-ray image during this experiment. Following the changes in the wires and finding the markers as the experiment proceeds, are fairly challenging. For instance, in some of the specimen circumferential markers were detached after few thousand cycles. Therefore, the marker needs to be ignored in all the sequences in order to maintain the consistency through all the cycles for the same specimen.

Another concern is that MRI analysis is subjective as well as observation based and therefore non-reproducible. The observer visual error is estimated to make 1 scale change in the grading system. In order to avoid this type of error, a three-dimensional software-based grading system would be beneficial to be replaced by the naked-eye observation-based grading system used for grading the level of tissue damage. Moreover, seeking a radiologist or physicians' opinion could potentially eliminate the source of observer error resulting by the lack of skill and experience of the examiner in reading the MRI images.

Degeneration grade of the cadaver discs is another major concern, since the relation between degeneration and disc herniation is still under question, however, all the specimens used in this study are reported as the

second grade of Pfirrmann classification of degeneration which can be interpreted as moderately degenerated discs (Pfirrmann et al. 2001) (See Appendix A). Likewise, it is believed that the geometry and consequently the biomechanical behavior of the degenerated disc is dissimilar to the healthy disc (Tsantrizos et al. 2005). A pioneer study by Adams et al. (1996) argued that the age and the level of degeneration which are clearly related to one another have a strong effect on stress distributions. Although according to the study by Schmidt et al (2007) it is assumed that there are no geometrical changes caused by degeneration, this assumption could be violated. Another complexity is that the wire grid may effect on the 6DoF biomechanical properties of the disc tissue (Korecki et al. 2008; Lee and Langrana, 1984). Therefore, the original study is designed to examine the effect of wire grid by measuring the stiffness and the phase angle for the control group.

Furthermore, limited access to hexapod and its complexities besides the wire grid insertion difficulties are other limitations for the coherent study. Disc curvatures due to the end plate natural shape, which sometimes makes the needle insertion problematic, therefore, the use of ultrasound or fluoroscopic imaging system could become necessary, occasionally. There are other likewise limitations which could not be avoided because of the nature of the study such as the absence of absence of biological tissue, ligaments and tendons and poor bone quality of the cadaver specimen due to their age.

4.4. Suggestions

Despite all technical limitations, the current study will be a pilot work for ongoing studies on three-dimensional internal disc strains using alternative methods under different loading scenarios. Comparing the scores coming from two different methods (MSS and MRI) supported by macroscopic analysis and correlating them statistically could potentially be done in future studies.

4.3.1. Different loading scenarios and increasing the dataset

The current study only examined the disc level of disc damage under combined flexion, right axial rotation and compression in seven cadaver specimens. More specimen would be required to confirm the correlation between MSS and MRI analyses. According to section 1.3, few studies have suggested that the disc undergoes a massive amount of strain under combined flexion, lateral bending and compression. Moreover, there might be a different initial failure site and mode of failure under other applied loading conditions; which could be helpful in understanding the mechanism of the disc herniation.

4.3.2.   Developing an MRI grading methodology/ Bone quality analysis

As discussed in section 4.3, a software-based robust MRI analysis could be beneficial to be replaced by the visual observation. Hereby the human error and some other limitations can be avoided. Moreover, since the bone quality can affect the mode of failure and longevity of the specimen during the experiment, a pre-evaluation of the bone using CT-scanner is suggested to be performed prior to the experiment.

4.3.3.   Regional biomechanical properties

Future studies also could be designed to examine the changes of regional fundamental biomechanical properties of the disc such as stiffness and phase angle before and after the disc failure. Six DoF analysis needs to be proceeded at 20,000 cycles or after the failure has occurred to confirm the tissue damage. Therefore, the analysis of the biomechanical properties could potentially support the findings from MSS and MRI analyses across all the anatomical regions. The disparity of mechanical properties in nine regions not only confirm the disc damage but also explains the biomechanical behavior of the disc after failure and hopefully would explain the findings from MSS analysis. This data also could be used for the comparison of wired and the control group in investigating the effect of wire grid insertion.

4.5. Conclusion

Chronic back pain is a benign, frequent, costly and complex condition which is the second leading cause of Burden of Disease in Australia. Lack of standard therapeutic treatment options for herniated disc and back pain, in general, is a consequence of the limited knowledge in understanding disc failure, although it is commonly believed that certain motions can cause disc herniation in the lumbar region of the vertebral column. It seems that more scientific studies are required to clarify the mode and mechanism of disc failure that results from certain repetitive motions such as manual handling and heavy lifting. A precise perusal of the literature reveals that the initiation of radial and circumferential tears and progression of three-dimensional internal maximum shear strains in anatomical disc regions, during repetitive combined loading is ambiguous up to the present time. Therefore, the current multimodal study was designed to investigate disc damage that results from combined motions under repetitive loading using internal tissue displacements and strains supported by clinical analysis based on MRI assessment.

Findings from this study reveal that the highest maximum shear strain is anatomically located where annular and circumferential tears are present in MRI image (grade 3). The concentration of MSS values in the annulus is statistically correlated with tears and fractures in posterior and posterolateral regions of the disc (Spearman correlation factor= 0.5966; P<0.001). Therefore, it can be concluded that MRI analysis is a complementary methodology which could be helpful in determining the level of damage in the disc. The right posterolateral region of the disc is experiencing the highest mean MSS (62%) under flexion (13 degrees), right axial rotation (2 degrees) and 1.7 MPa compression up to 20,000 cycles or failure. In addition, this loading condition can most possibly cause the annulus protrusion by forming the circumferential tears. Several other distinct modes of disc failure were also seen in this study which seems to be related to the cadaver bone quality and the level of degeneration such as nucleus extrusion, endplate fracture and bone crush fracture.

Finally, the result obtained from two different methods in this study and similar future studies would be valuable in terms of developing the current surgical methods and procedures, therapeutic implant designs to avoid therapy failure and improving the rehabilitation strategies and physical guidelines such as heavy lifting. Similar future studies are required to validate the FEA computational models and also to bring insight to tissue engineering.

References

1. ABS (Australian Bureau of Statistics) 2013a. Australian Health Survey: first results, cat. no. 4364.0.55.001. Canberra: ABS 122. 2010. viewed 23 Aug. 2017 <AIHW:http://www.aihw.gov.au/home/>

2. Adams, M.A., Green, T.P. and Dolan, P., 1994. The strength in anterior bending of lumbar intervertebral discs. Spine, 19(19), pp.2197-2203.

3. Adams, M.A., Mcnally, D.S. and Dolan, P., 1997. Stress Distributions Inside Intervertebral Discs. The Journal of Bone and Joint Surgery-british Volume, 79(3S), p.283.

4. AIHW. Australian Institution of Health and Welfare. Canberra: AIHW, 2010:Cat. no. AUS.

5. Amin, D.B., Lawless, I.M., Sommerfeld, D., Stanley, R.M., Ding, B. and Costi, J.J., 2015. Effect of potting technique on the measurement of six degree-of-freedom viscoelastic properties of human lumbar spine segments. Journal of biomechanical engineering, 137(5), p.054501.

6. Australian Institute of Health and Welfare 2016. Australian Burden of Disease Study: Impact and causes of illness and death in Australia 2011. Australian Burden of Disease Study series no. 3. BOD 4. Canberra: AIHW.

7. Beattie, P.K. and Meyers, S.P., 1998. Magnetic resonance imaging in the low back pain: General principles and clinical issues. Physical therapy, 78(7), p.738.

8. Berger-Roscher, N., Casaroli, G., Rasche, V., Villa, T., Galbusera, F. and Wilke, H.J., 2017. Influence of Complex Loading Conditions on Intervertebral Disc Failure. Spine, 42(2), pp.E78-E85.

9. Bogduk, N., 2005. Clinical anatomy of the lumbar spine and sacrum. Elsevier Health Sciences.

10. Callaghan, J.P. and McGill, S.M., 2001. Intervertebral disc herniation: studies on a porcine model exposed to highly repetitive flexion/extension motion with compressive force. Clinical Biomechanics, 16(1), pp.28-37.

11. Costi, J.J., Stokes, I.A., Gardner-Morse, M., Laible, J.P., Scoffone, H.M. and Iatridis, J.C., 2007. Direct measurement of intervertebral disc maximum shear strain in six degrees of freedom: motions that place disc tissue at risk of injury. Journal of biomechanics, 40(11), pp.2457-2466.

12. Costi, J.J., Stokes, I.A.F., Gardner-Morse, M., Laible, J.P., Scoffone, H.M. and Iatridis, J.C., 2009, May. Lateral Bending And Flexion Place Intervertebral Disc Tissue At Greatest Risk Of Injury.In Orthopaedic Proceedings (Vol. 91, No. SUPP II, pp. 350-350). Orthopaedic Proceedings.

13. Dhara Amin, Christina Moawad, Richard M Stanley, Boyin Ding and John J Costi, 2016, unpublished data.

14. Humzah, M.D. and Soames, R.W., 1988. Human intervertebral disc: structure and function. The Anatomical Record, 220(4), pp.337-356.

15. Jensen, M.C., Brant-Zawadzki, M.N., Obuchowski, N., Modic, M.T., Malkasian, D. and Ross, J.S., 1994. Magnetic resonance imaging of the lumbar spine in people without back pain. New England Journal of Medicine, 331(2), pp.69-73.

16. Kelsey, J.L., Githens, P.B., White, A.A., Holford, T.R., Walter, S.D., O'Connor, T., Ostfeld, A.M., Weil, U., Southwick, W.O. and Calogero, J.A., 1984. An epidemiologic study of lifting and twisting on the job and risk for acute prolapsed lumbar intervertebral disc. Journal of Orthopaedic Research, 2(1), pp.61-66.

17. Korecki, C.L., Costi, J.J. and Iatridis, J.C., 2008. Needle puncture injury affects intervertebral disc mechanics and biology in an organ culture model. Spine, 33(3), p.235.

18. Kumar, S., 1990. Cumulative load as a risk factor for back pain. Spine, 15(12), pp.1311- 1316.

19. Kuslich, S.D., Ulstrom, C.L. and Michael, C.J., 1991. The tissue origin of low back pain and sciatica: a report of pain response to tissue stimulation during operations on the lumbar spine using local anesthesia. The Orthopedic clinics of North America, 22(2), p.181.

20. Lee, C.K. and Langrana, N.A., 1984. Lumbosacral Spinal Fusion A Biomechanical Study. Spine, 9(6), pp.574-581.

21. Liu, Y.K., Njus, G., Buckwalter, J. and Wakano, K., 1983. Fatigue response of lumbar intervertebral joints under axial cyclic loading. Spine, 8(8), pp.857-865.

22. Mayerhoefer, M.E., Stelzeneder, D., Bachbauer, W., Welsch, G.H., Mamisch, T.C., Szczypinski, P., Weber, M., Peters, N.H., Fruehwald- Pallamar, J., Puchner, S. and Trattnig, S., 2012. Quantitative analysis of lumbar intervertebral disc abnormalities at 3.0 Tesla: value of T2 texture features and geometric parameters. NMR in biomedicine, 25(6), pp.866-872.

23. Paul Brinckmann, D., 1986. Injury of the Annulus Fibrosus and Disc Protrusions: An In Vitro Investigation on Human Lumbar Discs. Spine, 11(2), pp.149-153.

24. Pearcy, M., Portek, I.A.N. and Shepherd, J., 1984. Three-dimensional x-ray analysis of normal movement in the lumbar spine. *Spine*, *9*(3), pp.294-297.

25. Pfirrmann, C.W., Metzdorf, A., Zanetti, M., Hodler, J. and Boos, N., 2001. Magnetic resonance classification of lumbar intervertebral disc degeneration. Spine, 26(17), pp.1873-1878.

26. Qasim, M., Natarajan, R.N., An, H.S. and Andersson, G.B., 2014. Damage accumulation location under cyclic loading in the lumbar disc shifts from inner annulus lamellae to peripheral annulus with increasing disc degeneration. Journal of biomechanics, 47(1), pp.24-31.

27. Quittan, M., 2002. Management of back pain. Disability and rehabilitation, 24(8), pp.423- 434.

28. Rajasekaran, S., Bajaj, N., Tubaki, V., Kanna, R.M. and Shetty, A.P., 2014. Anatomy of Failure in Lumbar Disc Herniation. An In Vivo, Multimodal, Prospective Study of 181 Subjects. Global Spine Journal, pp.in3-01.

29. Raspe, H., Matthis, C., Croft, P., O'neill, T. and European Vertebral Osteoporosis Study

Group, 2004. Variation in back pain between countries: the example of Britain and Germany. Spine, 29(9), pp.1017-1021.

30. Ricketson, R., Simmons, J.W. and Hauser, B.O., 1996. The Prolapsed Intervertebral Disc: The High‐ Intensity Zone With Discography Correlation. Spine, 21(23), pp.2758-2762.

31. Schellhas, K.P., Pollei, S.R., Gundry, C.R. and Heithoff, K.B., 1996. Lumbar Disc High‐intensity Zone: Correlation of Magnetic Resonance Imaging and Discography. Spine, 21(1), pp.79-86.

32. Singel, T.C., Patel, M.M. and Gohil, D.V., 2004. A study of width and height of lumbar pedicles in Saurashtra region. J Anat Soc India, 53(1), pp.4-9.

33. Stokes, I.A., Gardner-Morse, M., Churchill, D. and Laible, J.P., 2002. Measurement of a spinal motion segment stiffness matrix. Journal of Biomechanics, 35(4), pp.517-521.

34. Tomaszewski, K.A., Saganiak, K., Gładysz, T. and Walocha, J.A., 2015. The biology behind the human intervertebral disc and its endplates. Folia Morphol (Warsz), 74, pp.157-168.

35. Tsantrizos, A., Ito, K., Aebi, M. and Steffen, T., 2005. Internal strains in healthy and degenerated lumbar intervertebral discs. Spine, 30(19), pp.2129-2137.

36. Vernon-Roberts, B., Fazzalari, N.L. and Manthey, B.A., 1997. Pathogenesis of Tears of the Anulus Investigated by Multiple‐ Level Transaxial Analysis of the T12‐ L1 Disc. Spine, 22(22), pp.2641-2646.

37. Vertebrae shape across various regions, Digital image, n.d. photograph, viewed 12 Oct. 2017, <http://what-when-how.com/wp-content/uploads/2012/08/tmp696717_thumb1.png>.

38. Wade, K.R., Robertson, P.A., Thambyah, A. and Broom, N.D., 2015. "Surprise" loading in flexion increases the risk of disc herniation due to annulus-endplate junction failure: a mechanical and microstructural investigation. Spine, 40(12), pp.891-901.

39. Wade, K.R., Schollum, M.L., Robertson, P.A., Thambyah, A. and Broom, N.D., 2016. ISSLS Prize Winner: Vibration Really Does Disrupt the Disc: A Microanatomical Investigation. Spine, 41(15), pp.1185-1198.

40. Wilder, D.G., Pope, M.H. and Frymoyer, J.W., 1988. The biomechanics of lumbar disc herniation and the effect of overload and instability. Clinical Spine Surgery, 1(1), pp.16-32.

41. Williams, F.M., Bansal, A.T., Van Meurs, J.B., Bell, J.T., Meulenbelt, I., Suri, P., Rivadeneira, F., Sambrook, P.N., Hofman, A., Bierma-Zeinstra, S. and Menni, C., 2013. Novel genetic variants associated with lumbar disc degeneration in northern Europeans: a meta-analysis of 4600 subjects. Annals of the rheumatic diseases, 72(7), pp.1141-1148.

42. Yu, Y., Cha, T.D., Moore, G., Mao, H., Tsai, T.Y., Li, J.S., Wood, K.B. and Li, G., 2016. Ranges of Cervical Intervertebral Disc Deformation during an In Vivo Dynamic Flexion‐ Extension of the Neck. The Spine Journal, 16(10), p.S259.

Abbreviations

MSS (Maximum Shear Strain); IVD (Intervertebral Disc); EPJF (Endplate Junction Failure); BoD (Burden of disease); DALYs (Disability-adjusted life years); AIHW (Australian Institute of Health and Welfare); ABS (Australian Bureau of Statistics); FSU (functional spinal units); MRI (magnetic resonance imaging); DoF (Degree of freedom); PMMA (Poly methyl methacrylate); PLL (posterior longitudinal ligament); FEA(finite element analysis); SD (standard deviation); CI (confidence intervals); IDD (inter-vertebral disc degeneration).

Keywords

Disc herniation; intervertebral disc; maximum shear strain; largest principal strain; biomechanical properties; three-dimensional; stereo radiography; Pfirrmann degeneration classification; nucleus extrusion; annulus protrusion; end plate fracture; disc prolapsed; rim lesion; concentric and radial tears.

Appendices

Appendix A. Pfirrmann disc degeneration MRI-based classification (Pfirrmann et al. 2001).

Grade	Structure	Distinction of Nucleus and Anulus	Signal Intensity	Height of Intervertebral Disc
I	Homogeneous, bright white	Clear	Hyperintense, isointense to cerebrospinal fluid	Normal
II	Inhomogeneous with or without horizontal bands	Clear	Hyperintense, isointense to cerebrospinal fluid	Normal
III	Inhomogeneous, gray	Unclear	Intermediate	Normal to slightly decreased
IV	Inhomogeneous, gray to black	Lost	Intermediate to hypointense	Normal to moderately decreased
V	Inhomogeneous, black	Lost	Hypointense	Collapsed disc space

* Modified from Pearce (cited by Eyre et al[9]).

Appendix B. Digitizing Process for specimen W25 (Neutral cycle) consisting of 5 steps for left and right x-radiology images: (a)recognition of 12 calibration beads (b) detecting 10 endplate beads (c) adding points to wires (12) (d) recognizing the disc periphery using 20 circumferential markers (e) saving all the landmarks to '.xdg' file format.
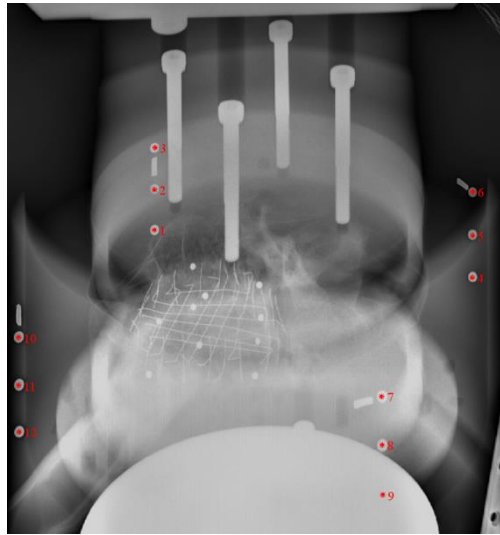
(a)
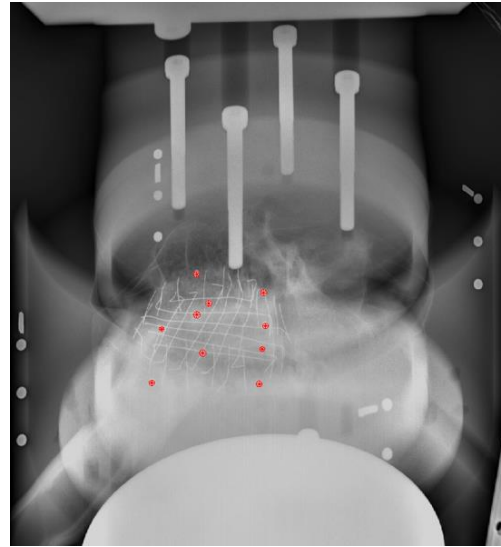
(b)
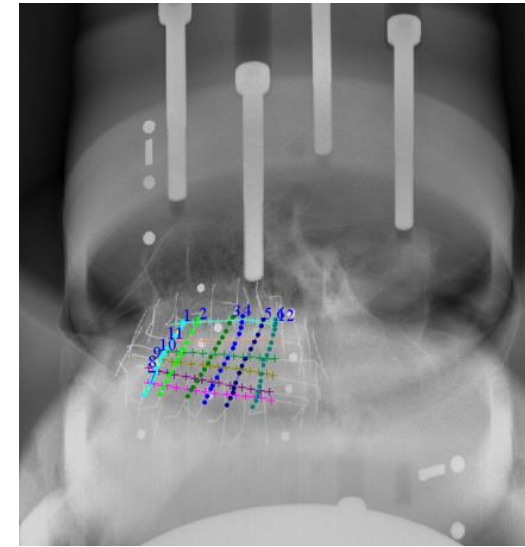
(c)
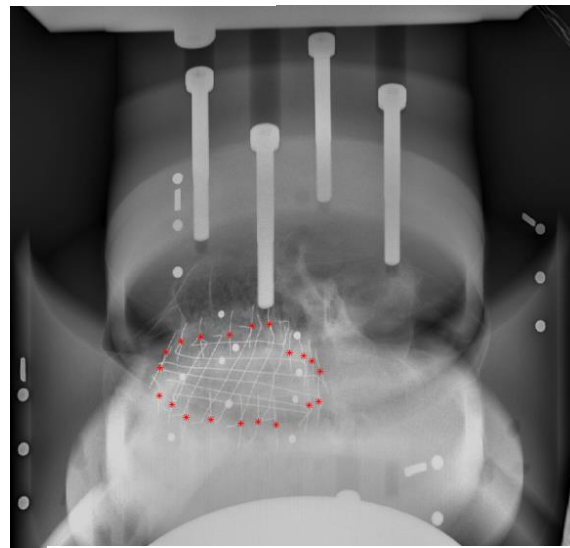
(d)
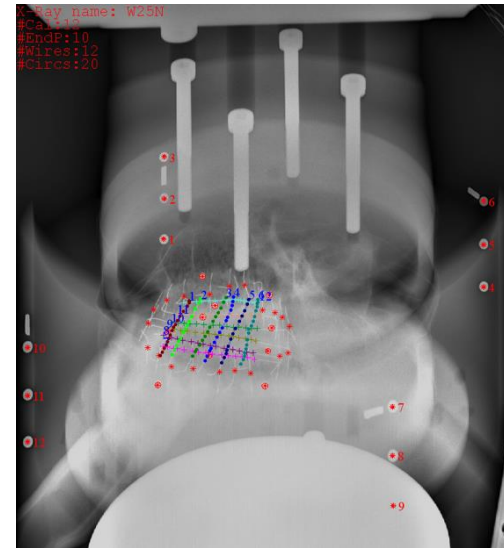
(e)

Appendix C. Digitizing Process: the optimum angle, Hungarian set and bad files recognized by both software and the user for all the specimens.

Speciman ID	Opt Angle	Hungarian set	Outliers	Redegitising required?	Bad file
W12N	32	1	4 outliers, 4 red intersections,w3 slightly spiky	No	1 7,1 8,1 12, 2 7
W12C1	30	2	3 outliers, 3 red intersections,w7	No	1 7,1 8, 1 12, 2 7
W12C500	57	1	2 outliers, 4 red intersections	No	1 7, 1 8
W12C1000	51	1	4 outliers, 2 red intersections, W2 &9	No	1 7, 1 8, 1 12, 2 7, 2 8, 6 9
W12C5000	-20	1	3 outliers, 4 red intersections	No	1 7, 1 8, 1 12, 2 7, 6 11
W12C10000	70	2	3 outliers, 5 red intersections	No	1 7, 1 8, 1 12, 2 7, 2 12, 3 7, 6 7, 6 11
W13N	38	1	4 outliers, 3 red intersections	No	1 7, 1 8, 1 12, 2 7
W13C1	52	1	4 outliers, 3 red intersections at W1&W9/11	Redigitised	1 7, 1 8, 1 9, 1 12
W13C500	80	1	6 outliers, W11 &12 can't get fixed	Redigitised	1 7, 1 8, 1 12, 2 7, 6 7,6 12
W15N	44	1	No outliers, 8 red intersections, W12 slightly unmatched between right and left	No	(999 999, 999 999)
W15C1	49	2	2 outliers, 5 red intersection	No	1 7, 1 8
W15C500	60	2	2 outliers, 6 red intersection, W4 &9 slightly spiky	No	1 7, 6 7
W15C1000	42	1	1 outlier, 7 red intersection, end of W12 with W8 is un-matched	No	1 7, 999 9999
W15C5000	38	1	1 outlier, 7 red intersection, end of W12slightly spiky	No	1 7, 999 999
W16N	27	2	4 outliers, 3 red intersections	No	1 7, 1 8, 2 7, 6 11
W16C1	39	1	5 outliers, 3 red intersections	No	1 7, 1 8, 1 9, 2 7, 6 11
W16C500	33	1	4 outliers, 2 red intersections, W11 slightly spiky	No	1 7, 1 8, 2 7, 3 7, 6 11
W16C1000	40	2	4 outliers	No	1 7, 1 8, 2 7, 6 11
W16C5000	61	1	4 outliers	Redigitised	1 7, 1 8, 2 7, 6 11
W16C10000	60	2	4 outliers	No	1 7, 1 8, 2 7, 6 11
W18N	30	1	4 outliers, 7 red intersections, end of W12 is spiky	No	1 8, 2 8, 4 8, 7 8
W18C1	37	1	3 outliers, w7 between W8 &10	No	1 8, 2 8, 7 8
W18C500	70	2	4 outliers, 8 red intersections	No	1 8, 2 8, 7 8, 12 7
W18C1000	39	1	4 outliers, 9 red intersections, spiky W10 and end of W12	No	1 8, 2 8, 7 8, 7 9
W18C5000	58	2	3 outliers, 9 red intersections, W1 is slightly spiky	No	2 8, 2 9, 7 8
W18C10000	66	1-Jan	3 outliers, 9 red intersections, W1 is slightly spiky	Redigitised	1 8, 1 9, 2 8
W21N	50	1	1 outlier, no red intersections, W12 &13 is slightly spiky	Redigitised	6 13, 999 999
W21C1	56	1	4 outliers, 1 red intersection, W6,10,11 were slightly spiky, W8 can't get fixed	Redigitised	1 7, 6 10, 6 8, 6 7
W21C500	32	1	2 outliers, W6 & 13 are slightly spiky	No	1 7, 6 7
W21C1000	60	1	4 outliers, W8,11,12 & 13 are slightly spiky	No	1 7, 2 7, 6 7, 6 8
W23N	42	2	3 outliers	No	1 6, 1 7, 2 6
W23C1	20	1	4 outliers, long end of W3 &4 couldn't get fix by redigitising	Redigitised	1 6, 1 7, 1 8, 2 6
W23C500	20	1	3 outliers	No	1 6, 1 7, 2 6
W23C1000	42	1	5 outliers	l (R and L jpeg files are labl	1 6,1 7, 1 8, 2 6, 3 6
W23C5000	43	2	3 outliers	No	1 6, 1 7, 2 6
W23C10000	40	2	4 outliers, Wire 8 is slightly spiky	No	1 6, 1 7, 2 6, 5 8
W23C15000	42	1	4 outliers, end of W8 is slightly spiky	No	1 6, 1 7, 2 6, 3 6
W23C20000	50	1	4 outliers	No	1 6, 1 7, 1 8, 2 6
W25N	25	1	1 outlier, end of W12 is slightly spiky	No	1 7,999 999
W25C1	25	2	1 outlier, spikes in W5 between W7 &8 is fixed	Redigitised	1 7,999 999
W25C500	60	2	No outliers, 13 red intersections	No	(999 999, 999 999)

Appendix D. Tissue displacement, largest principle strain, Maximum shear strain and MRI comparison table for all the specimens; The regions representing the highest maximum shear strain are highlighted.

D.1. Specimen: W12, final cycle=10,000

Regions	Tissue displacement (mm)	Largest Principle Strain (%)	Maximum Shear Strain (%)	MRI Score
Ant	1.9567	0.3574	55.17	3
Post	3.8523	0.3620	60.58	3
LAntL	1.7951	-0.2375	46.22	1
RAntL	1.3198	-0.2359	37.97	1
LLat	1.0888	0.1703	30.45	1
RLat	1.5981	-0.3962	58.78	2
LPosL	3.4724	0.2934	54.92	3
RPosL	3.5338	0.3885	76.08	3
Nuc	2.1992	-0.5221	87.01	3

Region	Tissue displacement (mm)									Largest Principle Strain (%)			Maximum Shear Strain (%)		
	Mean			SD			95% CI								
	dx	dy	dz	dx	dy	dz	dx	dy	dz	mean	sd	95ci	mean	sd	95ci
Ant	0.2239	0.1315	-1.9463	1.3698	0.5283	0.6741	0.6932	0.2673	0.3411	0.3574	0.1726	0.0874	55.17	21.11	10.68
Post	0.7072	-1.6553	3.4177	0.8480	0.4867	0.5783	0.4291	0.2463	0.2927	0.3620	0.0702	0.0355	60.58	15.4	7.8
LAntL	-0.5386	0.6439	-1.5965	0.8944	0.2194	0.4935	0.5285	0.1297	0.2916	-0.2375	0.0595	0.0352	46.22	15.14	8.95
RAntL	0.7404	-0.7105	-0.8310	0.4462	0.4414	0.5113	0.2637	0.2609	0.3022	-0.2359	0.1769	0.1046	37.97	23.53	13.9
LLat	0.9092	-0.4067	0.4499	0.7399	0.3915	0.4525	0.4186	0.2215	0.2560	0.1703	0.1059	0.0599	30.45	9.46	5.35
RLat	0.4621	-0.8630	1.2664	0.7731	1.8415	0.4619	0.4374	1.0419	0.2613	-0.3962	0.5182	0.2932	58.78	54.82	31.02
LPosL	0.9792	-1.8179	2.7972	0.6297	0.6864	0.6305	0.3298	0.3595	0.3303	0.2934	0.0764	0.0400	54.92	12.17	6.37
RPosL	0.4066	-0.2768	3.5902	1.3648	1.2820	0.5891	0.7149	0.6715	0.3086	0.3885	0.0636	0.0333	76.08	17.63	9.24
Nuc	-0.1372	-2.0103	0.8813	2.4822	2.4306	0.5145	1.2562	1.2301	0.2604	-0.5221	0.5140	0.2601	87.01	66.4	33.6

D.2. Specimen: W13, final cycle=500

Regions	Tissue displacement (mm)	Largest Principle Strain (%)	Maximum Shear Strain (%)	MRI Score
Ant	0.20736	0.3237	0.4573	1
Post	4.1813	0.4843	0.8843	3
LAntL	0.7078	-0.3828	0.6435	1
RAntL	1.8364	0.3152	0.3326	0
LLat	1.9390	0.2181	0.3642	1
RLat	3.67449	-0.7900	1.2896	3
LPosL	3.6945	0.4073	0.6270	1
RPosL	6.4892	-0.6641	1.2408	2
Nuc	2.0488	-0.3339	0.5835	1

Region	Tissue displacement (mm)									Largest Principle Strain (%)			Maximum Shear Strain (%)		
	Mean			SD			95% CI								
	dx	dy	dz	dx	dy	dz	dx	dy	dz	mean	sd	95ci	mean	sd	95ci
Ant	-0.1460	-0.1542	-0.0364	1.2077	0.4241	0.5156	0.6112	0.2146	0.2610	0.3237	0.1837	0.0930	45.73	18.54	9.38
Post	1.4548	-0.9350	3.8199	1.5139	0.9830	0.5058	0.7662	0.4975	0.2560	0.4843	0.1717	0.0869	88.43	42.7	21.61
LAntL	-0.5217	0.2538	-0.4157	1.2402	0.6036	0.3462	0.7329	0.3567	0.2046	-0.3828	0.2022	0.1195	64.35	14.75	8.72
RAntL	1.2539	0.2686	1.3273	0.4814	0.5500	0.4453	0.2845	0.3251	0.2631	0.3152	0.0637	0.0377	33.26	4.23	2.5
LLat	0.7006	-1.5207	1.0169	0.3477	0.5113	0.3816	0.1967	0.2893	0.2159	0.2181	0.0303	0.0171	36.42	12.6	7.13
RLat	-0.5921	2.1726	2.9179	2.4339	2.2647	0.3799	1.3771	1.2814	0.2150	-0.7900	0.9204	0.5207	128.96	103.76	58.71
LPosL	2.5020	-0.8392	2.6445	0.7177	1.1291	0.4992	0.3760	0.5914	0.2615	0.4073	0.0830	0.0435	62.7	9.73	5.09
RPosL	4.6761	-0.9743	4.4105	1.6666	1.8879	0.3908	0.8730	0.9889	0.2047	-0.6641	0.1519	0.0796	124.08	19.36	10.14
Nuc	0.7442	-0.2084	1.9778	0.9036	1.1037	0.4228	0.4573	0.5585	0.2140	-0.3339	0.1232	0.0624	58.35	14.04	7.11

D.3. Specimen: W15, final cycle=500

Regions	Tissue displacement (mm)	Largest Principle Strain (%)	Maximum Shear Strain (%)	MRI Score
Ant	4.7347	-0.6495	0.9521	3
Post	3.7492	-0.6145	1.0448	3
LAntL	4.7611	-0.5962	0.8826	2
RAntL	4.1893	-0.6241	0.9013	2
LLat	3.6737	-0.4408	0.6334	1
RLat	3.2422	-0.4521	0.5781	1
LPosL	3.6677	-0.4275	0.7010	2
RPosL	4.0883	0.6115	0.9699	3
Nuc	3.4646	-0.4588	0.4313	1

Region	Tissue displacement (mm)									Largest Principle Strain (%)			Maximum Shear Strain (%)		
	Mean			SD			95% CI			mean	sd	95ci	mean	sd	95ci
	dx	dy	dz	dx	dy	dz	dx	dy	dz						
Ant	-0.6384	0.4662	-4.6779	0.9979	0.2201	0.3254	0.4890	0.1078	0.1595	-0.6495	0.0495	0.0243	95.21	14.51	7.11
Post	-0.1326	3.1165	-2.0979	1.1387	2.1259	0.2598	0.5763	1.0759	0.1315	-0.6145	0.4771	0.2415	104.48	59.93	30.33
LAntL	0.5366	-0.1295	-4.7308	0.7073	0.4171	0.2279	0.4180	0.2465	0.1347	-0.5962	0.0392	0.0232	88.26	9.26	5.47
RAntL	0.2441	0.5207	-4.1536	0.6412	0.4290	0.2779	0.3789	0.2535	0.1642	-0.6241	0.0419	0.0248	90.13	10.18	6.01
LLat	0.1504	-0.2807	-3.6653	0.6269	0.7122	0.2634	0.3547	0.4030	0.1490	-0.4408	0.0297	0.0168	63.34	8.67	4.9
RLat	-0.2880	1.2779	-2.9758	0.5559	0.4269	0.2606	0.3145	0.2415	0.1474	-0.4521	0.0366	0.0207	57.81	8.91	5.04
LPosL	0.3714	2.7499	-2.4125	0.1866	1.7612	0.3270	0.0977	0.9226	0.1713	-0.4275	0.0849	0.0445	70.1	13.65	7.15
RPosL	-1.7024	3.6173	-1.7909	0.8924	2.2836	0.2822	0.4674	1.1962	0.1478	0.6115	0.2374	0.1244	96.99	28.64	15
Nuc	-1.0232	-0.0923	-3.3089	0.6742	0.6139	0.2745	0.3412	0.3107	0.1389	-0.4588	0.0530	0.0268	43.13	8.78	4.45

D.4. Specimen: W16, final cycle=10,000

Regions	Tissue displacement (mm)	Largest Principle Strain (%)	Maximum Shear Strain (%)	MRI score
Ant	2.02289	0.2733	0.4485	3
Post	1.8674	0.1765	0.3315	3
LAntL	2.37358	0.2105	0.4053	3
RAntL	1.93174	0.2381	0.3869	3
LLat	1.52141	-0.1461	0.2218	1
RLat	0.96498	0.1456	0.2309	2
LPosL	1.00024	-0.1307	0.2011	1
RPosL	0.87022	0.2733	0.3248	2
Nuc	1.2475	0.1765	0.2760	1

Region	Tissue displacement (mm)									Largest Principle Strain (%)			Maximum Shear Strain (%)		
	Mean			SD			95% CI			mean	sd	95ci	mean	sd	95ci
	dx	dy	dz	dx	dy	dz	dx	dy	dz						
Ant	0.7268	0.0690	-1.7638	0.9700	0.2840	0.1733	0.4909	0.1437	0.0877	0.2733	0.0813	0.0411	44.85	10.13	5.12
Post	1.7536	0.5575	-0.3548	0.6536	0.4248	0.1620	0.3308	0.2150	0.0820	0.1765	0.0637	0.0322	33.15	5.75	2.91
LAntL	1.3727	0.5138	-1.8742	0.4483	0.2154	0.1104	0.2649	0.1273	0.0652	0.2105	0.0385	0.0227	40.53	5.13	3.03
RAntL	1.2938	-0.2593	-1.4106	0.4332	0.3258	0.1536	0.2560	0.1926	0.0908	0.2381	0.0524	0.0310	38.69	6.6	3.9
LLat	0.4794	0.5737	-1.3348	0.4710	0.3018	0.1563	0.2665	0.1708	0.0885	-0.1461	0.0248	0.0141	22.18	6.02	3.4
RLat	0.5658	0.2065	-0.7658	0.3947	0.3074	0.1429	0.2233	0.1739	0.0808	0.1456	0.0686	0.0388	23.09	5.39	3.05
LPosL	0.6259	0.4464	-0.6552	0.3592	0.2523	0.1793	0.1882	0.1322	0.0939	-0.1307	0.0491	0.0257	20.11	4.96	2.6
RPosL	0.3949	0.7401	-0.2494	0.4514	0.7597	0.1377	0.2364	0.3980	0.0721	0.1857	0.0499	0.0261	32.48	5.09	2.66
Nuc	-0.676	-0.1309	-1.0410	0.5551	0.5520	0.1489	0.2809	0.2794	0.0754	-0.2558	0.1543	0.0781	27.6	12.35	6.25

D.5. Specimen: W18, final cycle=10,000

Regions	Tissue displacement (mm)	Largest Principle Strain (%)	Maximum Shear Strain(%)	MRI Score
Ant	3.8563	-0.4048	0.7031	3
Post	2.5132	0.2061	0.4077	1
LAntL	2.8622	-0.3337	0.3839	1
RAntL	4.3513	-0.4511	0.7914	3
LLat	1.3818	0.3487	0.4846	1
RLat	2.7909	-0.2767	0.3480	2
LPosL	2.1459	0.1829	0.3140	1
RPosL	1.8762	-0.1532	0.2715	1
Nuc	2.8337	-0.3524	0.5920	3

Region	Tissue displacement (mm)									Largest Principle Strain (%)			Maximum Shear Strain (%)		
	Mean			SD			95% CI								
	dx	dy	dz	dx	dy	dz	dx	dy	dz	mean	sd	95ci	mean	sd	95ci
Ant	0.2681	-0.6661	-3.7917	0.9511	0.2674	0.5615	0.4813	0.1353	0.2842	-0.4048	0.0634	0.0321	28.01	9.5	4.81
Post	0.3921	-2.3786	0.7430	0.4984	0.5392	0.4897	0.2522	0.2729	0.2478	0.2061	0.0591	0.0299	16.7	6.51	3.3
LAntL	0.3932	0.3828	-2.8105	1.1677	0.2806	0.4494	0.6901	0.1658	0.2656	-0.3337	0.0428	0.0253	28.52	3.09	1.83
RAntL	1.0742	-1.6345	-3.8999	0.5943	0.4329	0.4329	0.3512	0.2558	0.2558	-0.4511	0.0518	0.0306	25.91	2.61	1.54
LLat	0.3606	-1.0243	-0.8624	0.7582	0.7434	0.4387	0.4290	0.4206	0.2482	0.3487	0.1653	0.0935	55.03	42.01	23.77
RLat	0.3770	-1.8932	-2.0260	0.6568	0.1801	0.4263	0.3716	0.1019	0.2412	-0.2767	0.0351	0.0199	18.33	3.51	1.98
LPosL	-0.4046	-1.7844	1.1315	0.3838	0.3510	0.4788	0.2011	0.1839	0.2508	0.1829	0.0419	0.0219	68.19	26.09	13.67
RPosL	0.6657	-1.7541	0.0951	0.4991	0.3589	0.5803	0.2615	0.1880	0.3040	-0.1532	0.0497	0.0260	15.11	4.12	2.16
Nuc	-0.6075	-2.3767	-1.4309	1.3801	1.0412	0.4681	0.6984	0.5269	0.2369	-0.3524	0.1202	0.0608	13.36	6.42	3.25

D.6. Specimen: W23, final cycle=20,000

Regions	Tissue displacement (mm)	Largest Principle Strain (%)	Maximum Shear Strain (%)	MRI Score
Ant	1.9296	-0.1774	0.3512	1
Post	12.2167	-1.9580	2.6614	3
LAntL	1.6809	0.2353	0.3912	1
RAntL	2.0064	-0.1814	0.3138	1
LLat	1.0208	-0.1517	0.2153	1
RLat	1.1977	-0.2457	0.4079	2
LPosL	0.4276	0.1159	0.1715	2
RPosL	9.6829	-0.8883	1.6040	3
Nuc	2.0289	-0.7711	0.9565	3

Region	Tissue displacement (mm)									Largest Principle Strain (%)			Maximum Shear Strain (%)		
	Mean			SD			95% CI								
	dx	dy	dz	dx	dy	dz	dx	dy	dz	mean	sd	95ci	mean	sd	95ci
Ant	-0.1850	-0.0720	-1.9249	0.6305	0.1248	0.2071	0.3191	0.0632	0.1048	-0.1774	0.0143	0.0072	35.12	10.74	5.44
Post	9.4397	7.8662	-0.2208	7.3055	5.8794	0.1835	3.6971	2.9754	0.0929	-1.9580	0.9716	0.4917	266.14	128.13	64.84
LAntL	0.0508	0.2655	-1.6660	0.5146	0.2649	0.1582	0.3041	0.1565	0.0935	0.2353	0.0448	0.0265	39.12	4.92	2.9
RAntL	0.1287	-0.5759	-1.9255	0.5918	0.1610	0.1478	0.3497	0.0952	0.0874	-0.1814	0.0124	0.0073	31.38	5.17	3.05
LLat	-0.4913	0.3280	-0.8687	0.6649	0.2456	0.1902	0.3762	0.1390	0.1076	-0.1517	0.0589	0.0333	21.53	5.43	3.07
RLat	-0.1181	-0.0860	-1.1923	0.4082	0.7940	0.1808	0.2310	0.4492	0.1023	-0.2457	0.1126	0.0637	40.79	22.46	12.71
LPosL	-0.4264	0.0403	-0.0728	0.3505	0.1877	0.1742	0.1836	0.0983	0.0912	0.1159	0.0617	0.0323	17.15	6.54	3.42
RPosL	4.8863	8.4179	-0.4055	4.2278	3.1873	0.1746	2.2146	1.6696	0.0914	-0.8883	0.4415	0.2313	160.4	69.38	36.34
Nuc	1.3952	1.0637	-1.0306	2.4723	1.8386	0.1784	1.2511	0.9304	0.0903	-0.7711	0.5211	0.2637	95.65	54.3	27.48

D.7. Specimen: W25, final cycle=500

Regions	Tissue displacement (mm)	Largest Principle Strain (%)	Maximum Shear Strain (%)	MRI Score
Ant	1.2747	0.1792	0.2801	2
Post	1.1531	-0.1403	0.1670	1
LAntL	1.7503	0.1565	0.2852	2
RAntL	1.4542	0.1752	0.2591	1
LLat	2.0268	0.3227	0.5503	3
RLat	0.653	0.0967	0.1833	1
LPosL	2.6023	0.3989	0.6819	3
RPosL	0.6627	-0.0919	0.1511	1
Nuc	0.8786	-0.1216	0.1336	1

Region	Tissue displacement (mm)									Largest Principle Strain (%)			Maximum Shear Strain (%)		
	Mean			SD			95% CI								
	dx	dy	dz	dx	dy	dz	dx	dy	dz	mean	sd	95ci	mean	sd	95ci
Ant	0.5596	-0.9255	-0.6969	0.7321	0.4176	0.0657	0.3705	0.2113	0.0333	0.1792	0.0802	0.0406	0.2801	0.0950	0.0481
Post	0.5306	0.4511	-0.9240	0.2325	0.3464	0.0660	0.1177	0.1753	0.0334	-0.1403	0.0169	0.0086	0.1670	0.0651	0.0330
LAntL	1.3277	-0.7807	-0.9478	0.5155	0.0533	0.0500	0.3046	0.0315	0.0296	0.1565	0.0412	0.0244	0.2852	0.0309	0.0183
RAntL	0.3489	-1.3320	-0.4834	0.5973	0.2206	0.0374	0.3530	0.1304	0.0221	0.1752	0.0265	0.0157	0.2591	0.0261	0.0154
LLat	1.7037	-0.3440	-1.0563	2.2316	0.6935	0.0593	1.2626	0.3924	0.0335	0.3227	0.3200	0.1811	0.5503	0.4201	0.2377
RLat	-0.4576	-0.3814	-0.5359	0.2402	0.4806	0.0686	0.1359	0.2719	0.0388	0.0967	0.0380	0.0215	0.1833	0.0351	0.0198
LPosL	1.7840	1.5407	-1.1113	1.2534	1.3315	0.0412	0.6566	0.6975	0.0216	0.3989	0.2453	0.1285	0.6819	0.2609	0.1367
RPosL	0.0628	0.0196	-0.6645	0.2305	0.2594	0.0736	0.1207	0.1359	0.0386	-0.0919	0.0138	0.0072	0.1511	0.0412	0.0216
Nuc	-0.3461	-0.0201	-0.8119	0.3812	0.2603	0.0646	0.1929	0.1317	0.0327	-0.1216	0.0453	0.0229	0.1336	0.0642	0.0325

Appendix E. ANOVA statistical analysis using SPSS software.

Between-Subjects Factors

		Value Label	N
Disc Region	1	Anterior	147
	2	Posterior	105
	3	Left Anterolateral	77
	4	Right Anterolateral	77
	5	Left Lateral	84
	6	Right Lateral	84
	7	Left Posterolateral	98
	8	Right Posterolateral	98
	9	Nucleus	105

Descriptive Statistics

Dependent Variable: Maximum Shear Strain

Disc Region	Mean	Std. Deviation	N
Anterior	38.8901	20.25619	147
Posterior	57.1295	32.03788	105
Left Anterolateral	46.0581	17.03788	77
Right Anterolateral	42.4006	30.30558	77
Left Lateral	40.6418	22.76138	84
Right Lateral	46.6938	52.78397	84
Left Posterolateral	59.0826	21.97768	98
Right Posterolateral	62.4169	33.41840	98
Nucleus	44.3755	21.53771	105
Total	48.4907	30.21875	875

Levene's Test of Equality of Error Variances[a]

Dependent Variable: Maximum Shear Strain

F	df1	df2	Sig.
4.176	8	866	.000

Tests the null hypothesis that the error variance of the dependent variable is equal across groups.

a. Design: Intercept + Region

Tests of Between-Subjects Effects

Dependent Variable: Maximum Shear Strain

Source	Type III Sum of Squares	df	Mean Square	F	Sig.	Partial Eta Squared
Corrected Model	61921.681[a]	8	7740.210	9.105	.000	.078
Intercept	1994663.940	1	1994663.940	2346.372	.000	.730
Region	61921.681	8	7740.210	9.105	.000	.078
Error	736191.560	866	850.106			
Total	2855539.961	875				
Corrected Total	798113.241	874				

Tests of Between-Subjects Effects

Dependent Variable: Maximum Shear Strain

Source	Noncent. Parameter	Observed Power[b]
Corrected Model	72.840	1.000
Intercept	2346.372	1.000
Region	72.840	1.000
Error		
Total		
Corrected Total		

a. R Squared = .078 (Adjusted R Squared = .069)

b. Computed using alpha = .05

Estimated Marginal Means

1. Grand Mean

Dependent Variable: Maximum Shear Strain

Mean	Std. Error	95% Confidence Interval	
		Lower Bound	Upper Bound
48.632	1.004	46.662	50.603

Multiple Comparisons

Dependent Variable: Maximum Shear Strain

	(I) Disc Region	(J) Disc Region	Mean Difference (I-J)	Std. Error	Sig.
Bonferroni	Anterior	Posterior	-18.2395*	3.72549	.000
		Left Anterolateral	-7.1681	4.10163	1.000
		Right Anterolateral	-3.5105	4.10163	1.000
		Left Lateral	-1.7517	3.98790	1.000
		Right Lateral	-7.8038	3.98790	1.000
		Left Posterolateral	-20.1925*	3.80231	.000
		Right Posterolateral	-23.5268*	3.80231	.000
		Nucleus	-5.4855	3.72549	1.000
	Posterior	Anterior	18.2395*	3.72549	.000
		Left Anterolateral	11.0714	4.37454	.416
		Right Anterolateral	14.7289*	4.37454	.029
		Left Lateral	16.4878*	4.26809	.004
		Right Lateral	10.4357	4.26809	.529
		Left Posterolateral	-1.9531	4.09522	1.000
		Right Posterolateral	-5.2874	4.09522	1.000
		Nucleus	12.7540	4.02399	.057
	Left Anterolateral	Anterior	7.1681	4.10163	1.000
		Posterior	-11.0714	4.37454	.416
		Right Anterolateral	3.6576	4.69901	1.000
		Left Lateral	5.4164	4.60007	1.000
		Right Lateral	-.6357	4.60007	1.000
		Left Posterolateral	-13.0245	4.44014	.124
		Right Posterolateral	-16.3588*	4.44014	.009
		Nucleus	1.6826	4.37454	1.000
	Right Anterolateral	Anterior	3.5105	4.10163	1.000
		Posterior	-14.7289*	4.37454	.029
		Left Anterolateral	-3.6576	4.69901	1.000
		Left Lateral	1.7588	4.60007	1.000
		Right Lateral	-4.2932	4.60007	1.000
		Left Posterolateral	-16.6820*	4.44014	.007
		Right Posterolateral	-20.0163*	4.44014	.000
		Nucleus	-1.9749	4.37454	1.000
	Left Lateral	Anterior	1.7517	3.98790	1.000
		Posterior	-16.4878*	4.26809	.004
		Left Anterolateral	-5.4164	4.60007	1.000
		Right Anterolateral	-1.7588	4.60007	1.000
		Right Lateral	-6.0520	4.49896	1.000

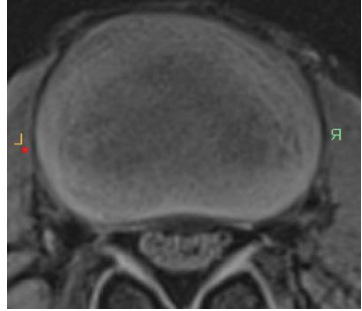**Multiple Comparisons**

Dependent Variable: Maximum Shear Strain

	(I) Disc Region	(J) Disc Region	Mean Difference (I-J)	Std. Error	Sig.
		Left Posterolateral	-18.4408*	4.33530	.001
		Right Posterolateral	-21.7751*	4.33530	.000
		Nucleus	-3.7337	4.26809	1.000
	Right Lateral	Anterior	7.9038	3.98790	1.000
		Posterior	-10.4357	4.26809	.529
		Left Anterolateral	.6357	4.60007	1.000
		Right Anterolateral	4.2932	4.60007	1.000
		Left Lateral	6.0520	4.49896	1.000
		Left Posterolateral	-12.3888	4.33530	.157
		Right Posterolateral	-15.7231*	4.33530	.011
		Nucleus	2.3183	4.26809	1.000
	Left Posterolateral	Anterior	20.1925*	3.80231	.000
		Posterior	1.9531	4.09522	1.000
		Left Anterolateral	13.0245	4.44014	.124
		Right Anterolateral	16.6820*	4.44014	.007
		Left Lateral	18.4408*	4.33530	.001
		Right Lateral	12.3888	4.33530	.157
		Right Posterolateral	-3.3343	4.16522	1.000
		Nucleus	14.7071*	4.09522	.013
	Right Posterolateral	Anterior	23.5268*	3.80231	.000
		Posterior	5.2874	4.09522	1.000
		Left Anterolateral	16.3588*	4.44014	.009
		Right Anterolateral	20.0163*	4.44014	.000
		Left Lateral	21.7751*	4.33530	.000
		Right Lateral	15.7231*	4.33530	.011
		Left Posterolateral	3.3343	4.16522	1.000
		Nucleus	18.0414*	4.09522	.000
	Nucleus	Anterior	5.4855	3.72549	1.000
		Posterior	-12.7540	4.02399	.057
		Left Anterolateral	-1.6826	4.37454	1.000
		Right Anterolateral	1.9749	4.37454	1.000
		Left Lateral	3.7337	4.26809	1.000
		Right Lateral	-2.3183	4.26809	1.000
		Left Posterolateral	-14.7071*	4.09522	.013
		Right Posterolateral	-18.0414*	4.09522	.000
Tamhane	Anterior	Posterior	-18.2395*	3.54496	.000
		Left Anterolateral	-7.1681	2.56149	.186

Multiple Comparisons

Dependent Variable: Maximum Shear Strain
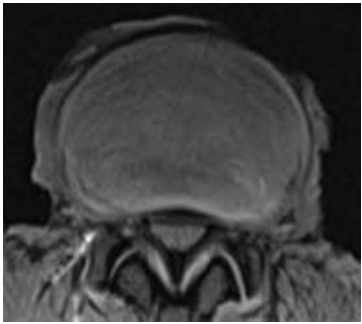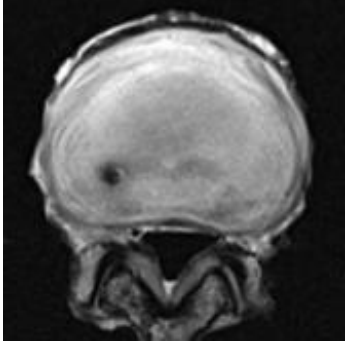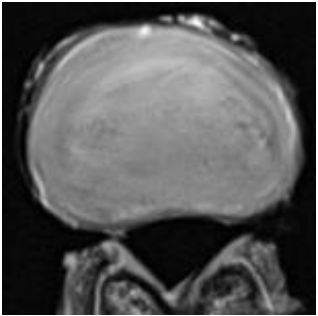
(I) Disc Region	(J) Disc Region	Mean Difference (I-J)	Std. Error	Sig.
	Right Anterolateral	-3.5105	3.83652	1.000
	Left Lateral	-1.7517	2.99314	1.000
	Right Lateral	-7.8038	5.99664	1.000
	Left Posterolateral	-20.1925*	2.77849	.000
	Right Posterolateral	-23.5268*	3.76657	.000
	Nucleus	-5.4855	2.68497	.789
Posterior	Anterior	18.2395*	3.54496	.000
	Left Anterolateral	11.0714	3.68042	.104
	Right Anterolateral	14.7289	4.65896	.065
	Left Lateral	16.4878*	3.99288	.002
	Right Lateral	10.4357	6.55316	.987
	Left Posterolateral	-1.9531	3.83461	1.000
	Right Posterolateral	-5.2874	4.60123	1.000
	Nucleus	12.7540*	3.76740	.031
Left Anterolateral	Anterior	7.1681	2.56149	.186
	Posterior	-11.0714	3.68042	.104
	Right Anterolateral	3.6576	3.96202	1.000
	Left Lateral	5.4164	3.15240	.963
	Right Lateral	-.6357	6.07770	1.000
	Left Posterolateral	-13.0245*	2.94936	.001
	Right Posterolateral	-16.3588*	3.89433	.002
	Nucleus	1.6826	2.86144	1.000
Right Anterolateral	Anterior	3.5105	3.83652	1.000
	Posterior	-14.7289	4.65896	.065
	Left Anterolateral	-3.6576	3.96202	1.000
	Left Lateral	1.7588	4.25395	1.000
	Right Lateral	-4.2932	6.71536	1.000
	Left Posterolateral	-16.6820*	4.10565	.003
	Right Posterolateral	-20.0163*	4.82944	.002
	Nucleus	-1.9749	4.04295	1.000
Left Lateral	Anterior	1.7517	2.99314	1.000
	Posterior	-16.4878*	3.99288	.002
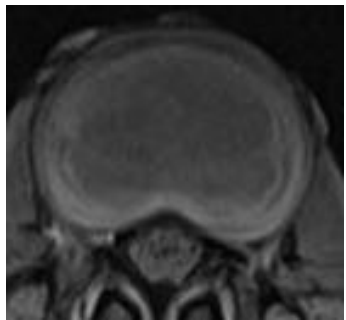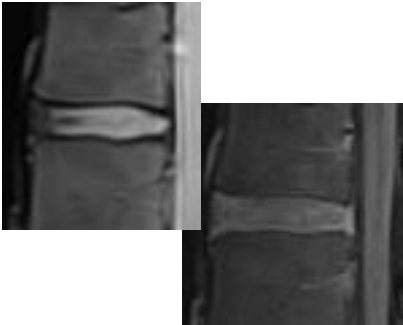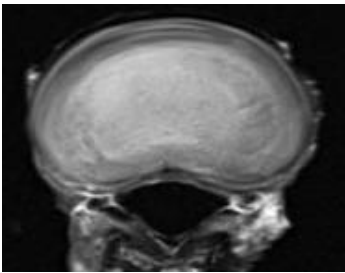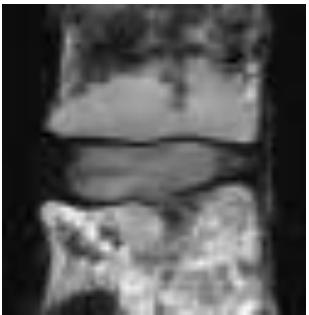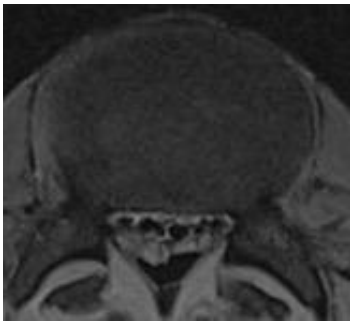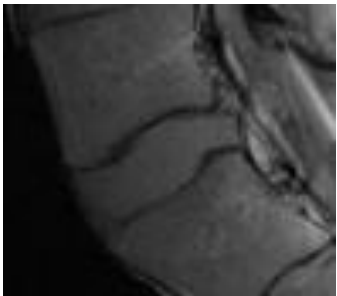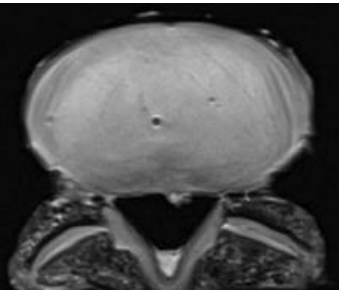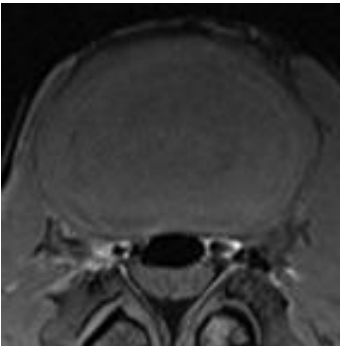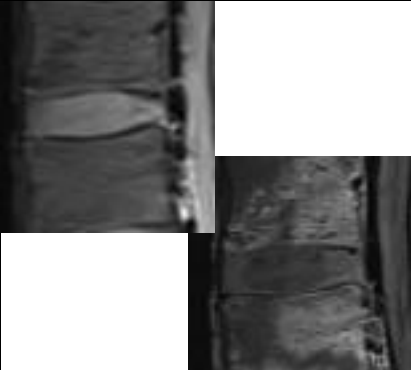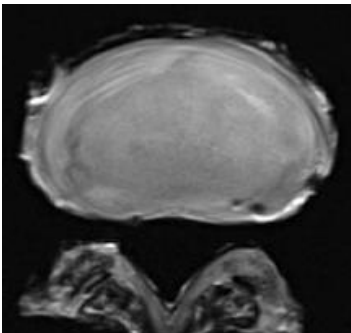
Multiple Comparisons
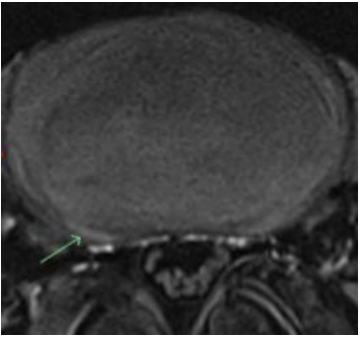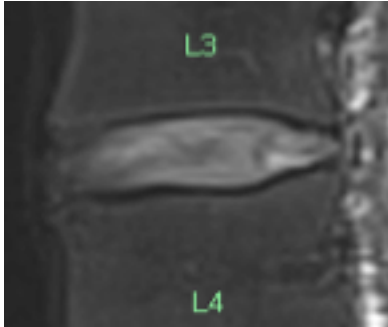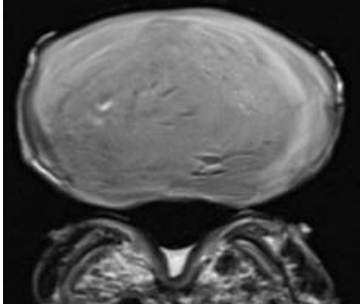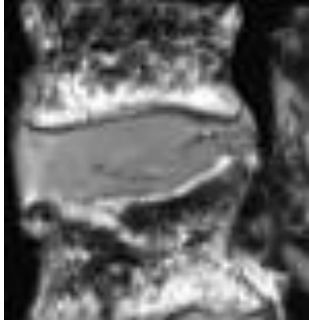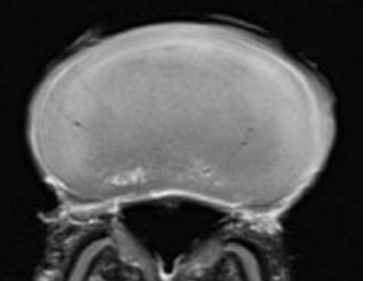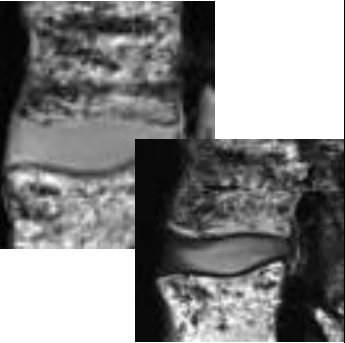
Dependent Variable: Maximum Shear Strain

(I) Disc Region	(J) Disc Region	Mean Difference (I-J)	Std. Error	Sig.
	Left Anterolateral	-5.4164	3.15240	.963
	Right Anterolateral	-1.7588	4.25385	1.000
	Right Lateral	-6.0520	6.27185	1.000
	Left Posterolateral	-18.4408*	3.33112	.000
	Right Posterolateral	-21.7751*	4.19087	.000
	Nucleus	-3.7337	3.25353	1.000
Right Lateral	Anterior	7.8038	5.99664	1.000
	Posterior	-10.4357	6.55316	.987
	Left Anterolateral	.6357	6.07770	1.000
	Right Anterolateral	4.2932	6.71536	1.000
	Left Lateral	6.0520	6.27185	1.000
	Left Posterolateral	-12.3888	6.17229	.825
	Right Posterolateral	-15.7231	6.67564	.516
	Nucleus	2.3183	6.13076	1.000
Left Posterolateral	Anterior	20.1925*	2.77849	.000
	Posterior	1.9531	3.83461	1.000
	Left Anterolateral	13.0245*	2.94936	.001
	Right Anterolateral	16.6820*	4.10565	.003
	Left Lateral	18.4408*	3.33112	.000
	Right Lateral	12.3888	6.17229	.825
	Right Posterolateral	-3.3343	4.04037	1.000
	Nucleus	14.7071*	3.05722	.000
Right Posterolateral	Anterior	23.5268*	3.76657	.000
	Posterior	5.2874	4.60123	1.000
	Left Anterolateral	16.3588*	3.89433	.002
	Right Anterolateral	20.0163*	4.82944	.002
	Left Lateral	21.7751*	4.19087	.000
	Right Lateral	15.7231	6.67564	.516
	Left Posterolateral	3.3343	4.04037	1.000
	Nucleus	18.0414*	3.97664	.000
Nucleus	Anterior	5.4855	2.68497	.789
	Posterior	-12.7540*	3.76740	.031

Appendix F. Clinical analysis based on Pre- and Post- MRI images; a grading system was established to score the level of tissue damage within the nine anatomical disc regions. Specimen W21 was excluded later due to some technical errors in digitizing process (For interpretation of MRI images please refer to the online submitted version of this report).

Specimen ID	Pre-MRI		Post-MRI	
	Axial	Sagittal	Axial	Sagittal
W12				
W13				

W15				
W16				
W18				

W21				
W23				
W25				